Analysis and Suppression on Tower Vibration of Permanent Magnet Synchronous Generator-based Wind Energy Conversion System

Feihang Zhou, Ji Pang, Bo Wang, and Jianxiang Yang

***Abstract*—This study explores tower vibrations in large-scale permanent magnet synchronous generator (PMSG)-based wind energy conversion system (WECS). First, the aerodynamic characteristics of wind turbines, including wind shear (WS), tower shadow effect (TSE), and blade airfoil structure, are examined. Then, a mechanism model of tower vibration is established, and the impacts of WS and TSE on tower vibration are analyzed. Suppression schemes, including crossing resonance zone method and tower damping control, are evaluated, and a robust variable-pitch strategy based on sliding mode control is proposed to mitigate tower vibration. Comparative analysis suggests that the proposed strategy outperforms the crossing resonance zone method and the tower damping control in achieving more effective tower vibration suppression and reducing the influence of the 3p frequency component. The effectiveness of the model and algorithm is verified through simulation experiments.**

***Index Terms*—Tower vibration, PMSG-based WECS, WS, TSE, crossing resonance zone method, tower damping control, variable-pitch based on sliding mode control.**

NOMENCLATURE

A. Abbreviations

PMSG	permanent magnet synchronous generator
WECS	wind energy conversion system
WS	wind shear
TSE	tower shadow effect
TSR	tip-speed ratio
DMSD	double mass spring damping
MPPT	maximum power point tracking
MSC	machine-side converter
PSD	power spectral density

B. Variables

v / v_{hub}	wind speed/wind speed at the hub
v_{shear} / v_{tower}	wind speed changes caused by WS/TSE
θ_i	azimuth angle where $i=1,2,3$
r	radial distance from rotor axis
H	hub height
d	tower radius
x	distance from the blade origin to the tower midline
μ	wind shear exponent
R / r_{hub}	wind wheel radius/hub radius
$I/\alpha/\beta$	inflow angle/attack angle/pitch angle
a/b	axial induction factor/tangential induction factor
λ / λ_{opt}	TSR/optimal value of TSR
ω_{tur} / ω_{gen}	wind turbine speed/generator speed
W	synthetic wind speed
F_{D} / F_{L}	aerodynamic drag/lift on blade element
C_{D} / C_{L}	drag/lift coefficients
R_{e} / M_{a}	Reynolds number/Mach number
C_{n} / C_{t}	normal force/tangential force coefficients
B/L	blades number/airfoil chord length
C_{P} / $C_{\text{P\_max}}$	wind energy utilization coefficient/the maximum value of wind energy utilization coefficient
$F_{\text{AD}i}$ / $F_{\text{AL}i}$	aerodynamic normal force/tangential force on the i-th blade
J_{tur} / J_{gen}	inertia moments of wind turbine/generator
T_{tur} / T_{gen}	wind turbine torque/generator torque
D_{s} / K_{s} / θ_{s}	damping coefficient/stiffness coefficient /twist angle of flexible drive-train

Received: July 5, 2024
Accepted: December 13, 2024
Published Online: May 1, 2025

Feihang Zhou is with the School of Automation, Xi'an University of Posts & Telecommunications, Xi'an 710061, China, and the School of Electrical Engineering, Xi'an University of Technology, Xi'an 710054, China (e-mail: zhoufeihang@xupt.edu.cn).

Ji Pang (corresponding author) and Bo Wang are with the School of Automation, Xi'an University of Posts & Telecommunications, Xi'an 710061, China (e-mail: pangji@xupt.edu.cn; wangbo_chen@126.com).

Jianxiang Yang is with the School of Automation, Guangdong Polytechnic Normal University, Guangzhou 510405, China (e-mail: yangjianxiang0108@126.com).

DOI: 10.23919/PCMP.2024.000083

M_1 / M_2	mass coefficients of tower-top mass block /tower-bottom mass block
D_T / K_T	damping coefficient/stiffness coefficient of tower
y_{X1} / y_{X2}	fore-aft displacements of tower-top mass block/tower-bottom mass block
ζ_X / ζ_Y	displacement differences in fore-aft direction/side-to-side direction
F_X / F_Y	fore-aft reaction forces from the tower base in fore-aft direction/side-to-side direction
y_{Y1} / y_{Y2}	side-to-side displacements of tower-top mass block/tower-bottom mass block
i_{sd} / i_{sq}	d/q-axis stator currents
u_{sd} / u_{sq}	d/q-axis stator voltages
L_{sd} / L_{sq}	d/q-axis stator inductances
R_s	stator resistance
n_p	pole logarithms
ψ	permanent magnet flux linkage
i_{gd} / i_{gq}	d/q-axis grid-side currents
u_{gd} / u_{gq}	d/q-axis grid-side voltages
ω_g	electric angular frequency of grid
L_{gd} / L_{gq}	d/q-axis grid-side inductances
R_g	grid-side resistance
E_{gd} / E_{gq}	d/q-axis voltage components of point of common coupling
T_{ref}	reference torque
T_{Damp}	damping compensation torque
ϑ	initial azimuth angle
ρ	air density
ω_0	angular frequency at the crossing point
F	bound of uncertainty
η	approaching rate of sliding mode surface
a_0	positive regulatory factor

I. Introduction

As a type of clean energy, wind energy has increasingly become more valued, given the aggravation of the environmental problems and the shortages of resources [1]–[3]. In recent years, the capacity and size of wind energy conversion systems (WECS) have grown significantly to capture more wind energy [4]–[7]. However, as the WECS capacity increases, the tower, as an important component of the unit, becomes more susceptible to high-intensity vibrations [8]–[10]. This can cause shutdown protection when the vibration amplitude exceeds the threshold and seriously affect the generation efficiency of wind turbines. Tower vibrations can also induce fatigue, potentially resulting in catastrophic tower collapses. As shown in Fig. 1, multiple collapse accidents of wind turbines have occurred in recent years.

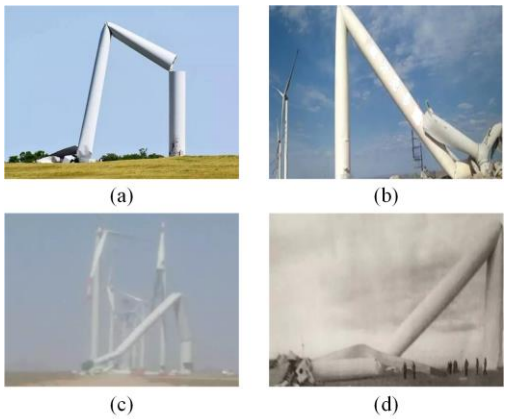

Fig. 1. Multiple wind turbine accidents in recent years. (a) Collapse accident in Oklahoma, the United States, in May 2019. (b) Collapse accident in Xinjiang in July 2017. (c) Collapse accident in Gansu in April 2019. (d) Collapse accident in Ningxia in December 2017.

Given the tower's large slenderness ratio, its flexibility should be accounted for. In addition, the tower's inherent damping is typically small, while continuous reductions in tower weight cause its natural frequency to further decrease. As a result, resonance may occur during wind turbine operations.

Changes in aerodynamic normal force and tangential force on the blade wheel are generally considered the primary contributors to tower vibrations, including fore-and-aft and side-to-side tower vibrations. However, the parameters that affects the tower vibrations are complex [11]–[13], which include wind shear (WS), tower shadow effect (TSE), and various uncontrollable elements like weather conditions, grid voltage dips, and grid voltage imbalance. Unlike these highly unpredictable factors, WS and TSE have a certain regularity, and their influence becomes increasingly pronounced with the large-scale development of wind turbines. Tower vibrations caused by WS and TSE can aggravate tower fatigue, increasing the risk of collapse.

Given the potential aggravation to tower fatigue and adverse impact on both the tower's service life and the normal operation of wind turbines, tower vibrations should be systematically analyzed and studied. Numerous studies have been conducted on the monitoring, analysis, and control of tower vibration. For example, reference [14] presents a method that actively controls the side-to-side tower vibration using generator torque, while simultaneously reducing fluctuations in the output power. Reference [15] studies wind turbine tower vibration control under random wind load, simulating the tower as a non-uniform Euler-Bernoulli beam system with parameter distribution based on the Hamiltonian principle and proposing a boundary control method

based on disturbance observer to suppress the tower vibration. In [16], the tower is regarded as a switching system composed of multiple sub-modules, and system stability is analyzed based on the switching principle and characteristic analysis method. Reference [17] proposes a modal parameter identification method for tower vibration to observe the global dynamic characteristics of tower vibration in emergency braking, while reference [18] proposes an operation mode analysis technology based on error measurement and covariance-driven approximation to identify the tower vibration mode and effectively estimate vibration damping. Reference [19] proposes the use of a tuned mass damper fluid-inverter for vibration control of spar-type offshore wind turbine towers, and reference [20] explores the impact of passive oscillations on power and wake for various yawing scenarios and proposes a yaw correction to improve turbine power output. Experimental results show that power output may increase with small amplitude oscillations. Reference [21] optimizes the shape memory alloy-based tuned mass dampers to control the seismic responses of wind turbine towers, while reference [22] proposes a control scheme balancing power generation and tower vibration reduction, which can achieve a notable reduction in tower vibrations with minimal impact on generated power. More researches on tower vibration suppression have been undertaken, such as [23]–[26].

While these studies have theoretical significance and practical application value, few studies have thoroughly investigated the underlying mechanism of tower vibration. To better understand the mechanism of tower vibration, it is necessary to comprehensively consider its mechanism model, complex working conditions, and current control strategies, rather than engaging in blind research. Furthermore, while WS and TSE are direct causes of tower vibration, there is no literature exploring the influence of WS and TSE on tower vibration and the ensuing vibration mechanism. Therefore, the primary motivation of this paper is to investigate the mechanism of tower vibration, analyze the impact of WS and TSE on tower vibration, and devise effective measures for vibration suppression.

This paper begins by examining the mechanism modeling of tower vibration in permanent magnet synchronous generator (PMSG)-based WECS, followed by an in-depth analysis of the influence laws of WS and TSE on tower vibration. Various schemes are then proposed to effectively suppress tower vibration. The main contributions of this paper are as follows:

1) The tower vibration mechanism is comprehensively analyzed, which includes the establishment of the tower vibration mechanism model, exploration of the causes of tower vibration, and identification of the key factors impacting tower vibration.

2) The influence laws of WS and TSE on tower vibration are revealed. The study finds that the 3p frequency component formed by WS and TSE induces tower resonance, particularly when the WECS is operating at specific speeds.

3) Various suppression schemes for tower vibration are analyzed. A robust variable-pitch strategy based on sliding mode control is then proposed to effectively manage tower vibration. Compared with the crossing resonance zone method and the tower damping control, the proposed strategy can more effectively suppress tower vibration and mitigate the influence of the 3p frequency component.

The rest of this paper is organized as follows. Section II discusses the aerodynamic characteristics of wind turbines including the WS and TSE, and the blade airfoils. Section III explores the PMSG-based WECS model consisting of the wind turbine model, the tower model, the flexible drive-train model, and the electrical system model. In Section IV, torque control of the PMSG-based WECS is described and tower vibration is thoroughly examined. Section V investigates various suppression methods of tower vibration including the crossing resonance zone method, the tower damping control, and the proposed robust variable-pitch strategy. Simulation results are discussed in Section VI, analyzing the performance and validity of these suppression methods. Finally, Section VII concludes the study.

II. Wind Turbine Aero-dynamic Characteristics

The aerodynamic characteristics of large-scale WECS are not simply dependent on the blade airfoil structure but are also susceptible to the influence of WS and TSE. Therefore, all of the blade airfoil, WS, and TSE should be considered when analyzing wind turbine's aerodynamic characteristics.

A. WS and TSE

In general, variations in the wind vector along the vertical direction form the vertical WS. When the blades pass the tower, airflow in front of the tower may be redirected, affecting the wind turbine [27], [28]. TSE is formed where the tower interferes with the airflow passing through the blades. WS and TSE can cause uneven airflow distribution, pulsation of mechanical torque of wind turbines, and reduction of power generation performance. The 3p frequency component caused by WS and TSE can continuously excite WECS at a relatively stable frequency [29], [30].

With the further increase in the diameter of large-scale wind turbines, the phenomena of WS and TSE have intensified. Considering WS and TSE, the

influence of shear wind and tower shadow wind on blade elements [32]–[34] can be described as:

$$v_{\text{shear}}(r,\theta_i)\approx v_{\text{hub}}\left[\begin{array}{l}\mu\left(\dfrac{r}{H}\right)\cos\theta_i+\dfrac{\mu(\mu-1)}{2}\left(\dfrac{r}{H}\right)^2\cos^2\theta_i+\\ \dfrac{\mu(\mu-1)(\mu-2)}{6}\left(\dfrac{r}{H}\right)^3\cos^3\theta_i\end{array}\right] \tag{1}$$

$$v_{\text{tower}}(r,\theta_i)\approx v_{\text{hub}}md^2\frac{r^2\sin^2\theta_i-x^2}{\left(r^2\sin^2\theta_i+x^2\right)^2} \tag{2}$$

where the azimuth angle $\theta_i(i=1,2,3)$ meets $\theta_{i+1}=\theta_i+120°$ and m meets $m=1+\mu(\mu-1)R^2/(8H^2)$ in [30]. The wind speed of the blade element can be written as:

$$v_i=v_{\text{hub}}+v_{\text{shear}}(r,\theta_i)+v_{\text{tower}}(r,\theta_i) \tag{3}$$

B. Aero-dynamic Characteristics of Blade Airfoil

Figure 2(a) shows the vector graph of the blade element. The inflow angle I and attack angle α are as follows:

$$I=\tan^{-1}\left[\frac{(1-a)v}{(1+b)R\omega_{\text{tur}}}\right]=\tan^{-1}\left[\frac{(1-a)}{(1+b)\lambda}\right] \tag{4a}$$

$$\alpha=\frac{180°}{\pi}I-\beta \tag{4b}$$

where the TSR meets $\lambda=R\omega_{\text{tur}}/v$.

In this paper, the airfoil curve of DU91-W2-250 shown in Fig. 2(b) is imported into the XFOIL software to calculate the lift coefficient $C_{\text{L}}(a)$ and drag coefficient $C_{\text{D}}(a)$, which are the functions of the attack angle α (Reynolds number $R_{\text{e}}=2\times10^6$ and Mach number $M_{\text{a}}=0.2$). The final results are illustrated in Fig. 2(c). As shown in Fig. 2(d), the resulting data can be estimated by using a linear fit scheme.

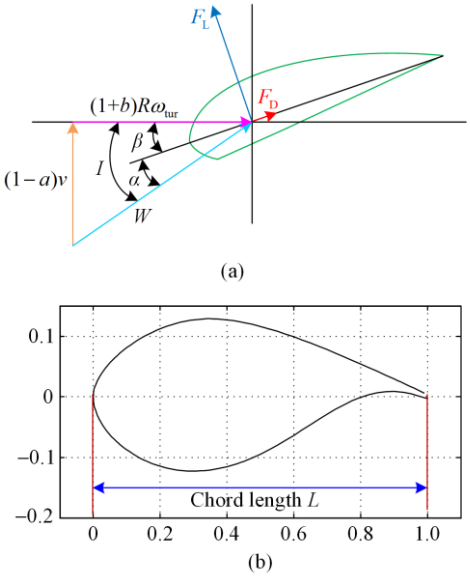

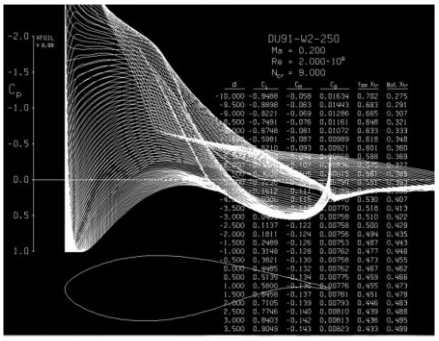

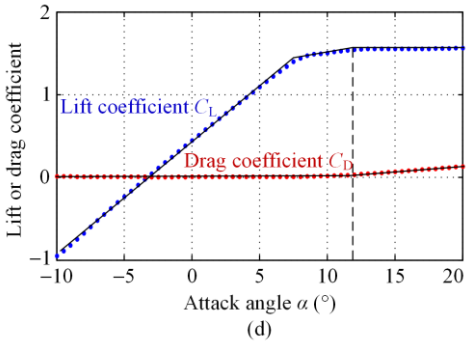

Fig. 2. Blade airfoil structure and the calculation lift and drag coefficients. (a) Blade element vector graph. (b) Airfoil curve. (c) Calculation results of the lift coefficient and drag coefficient in the XFOIL software. (d) The variation diagram of lift coefficient and drag coefficient with the attack angle.

Using linear fitting calculation, the equation is expressed as:

$$C_{\text{L}}(a)=\begin{cases}k_{\text{L1}}a+C_{\text{L1}}, & a\leqslant7.5°\\ k_{\text{L2}}a+C_{\text{L2}}, & 7.5°<a\leqslant12°\\ k_{\text{L3}}a+C_{\text{L3}}, & a>12°\end{cases} \tag{5a}$$

$$C_{\text{D}}(a)=\begin{cases}k_{\text{D1}}a+C_{\text{D1}}, & a\leqslant12°\\ k_{\text{D2}}a+C_{\text{D2}}, & a>12°\end{cases} \tag{5b}$$

where k_{L1}=0.1267; C_{L1}=0.45; k_{L2}=0.0356; C_{L2}=1.1328; k_{L3}=0; C_{L3}=1.56; k_{D1}=0; C_{D1}=0; k_{D2}=0.0169; C_{D2}=–0.2028.

The normal force coefficient C_{n} and tangential force coefficient C_{t} are defined as:

$$C_{\text{n}}=C_{\text{L}}(a)\cos I+C_{\text{D}}(a)\sin I \tag{6a}$$

$$C_{\text{t}}=C_{\text{L}}(a)\sin I-C_{\text{D}}(a)\cos I \tag{6b}$$

According to the blade element momentum theory, the induction factors a and b are given by:

$$a=\frac{g_1}{1+g_1} \tag{7a}$$

$$b=\frac{g_2}{1-g_2} \tag{7b}$$

where $g_1=\sigma C_{\text{n}}/(4\sin^2 I)$ and $g_2=\sigma C_{\text{t}}/(4\sin I\cos I)$, with $\sigma=BL/(2\pi r)$. In general, the induction factors a and b need the iterative solution, and the process is shown in Fig. 3(a). The wind energy utilization coefficient C_{P} can be given by:

$$C_{\mathrm{P}} = 4a(1-a)^2 \tag{8}$$

When $a = 1/3$, C_{P} can reach its maximum value of 16/27 (Betz limit). Furthermore, the C_{P}-λ curve is shown in Fig. 3(b). The maximum wind energy utilization coefficient $C_{\mathrm{P\_max}}$ is the Betz limit value since the aerodynamic losses are not considered in this paper. When $\beta = 0$, the optimal TSR λ_{opt} is equal to 8.

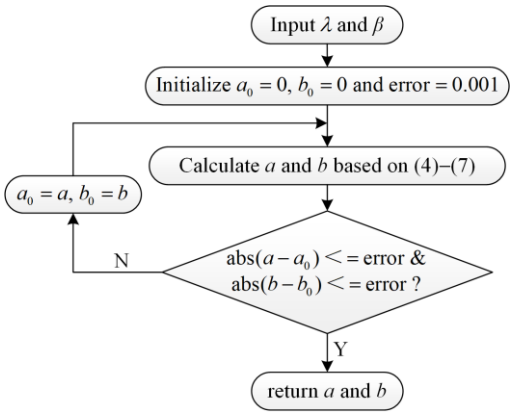

(a)

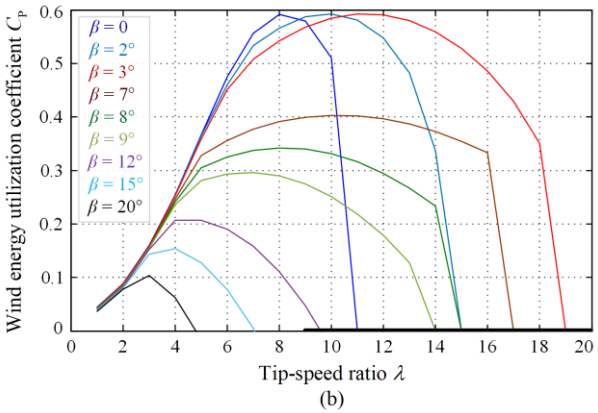

(b)

Fig. 3. Calculations of induction factors and wind turbine power coefficient. (a) Induction factors calculation flow chart. (b) Relationship curve between the wind energy utilization coefficient and the tip speed ratio.

III. Mathematical Model of PMSG-based WECS

As presented in Fig. 4, the PMSG-based WECS model consists of the wind turbine model, the tower model, the flexible drive-train model, and the electrical system model.

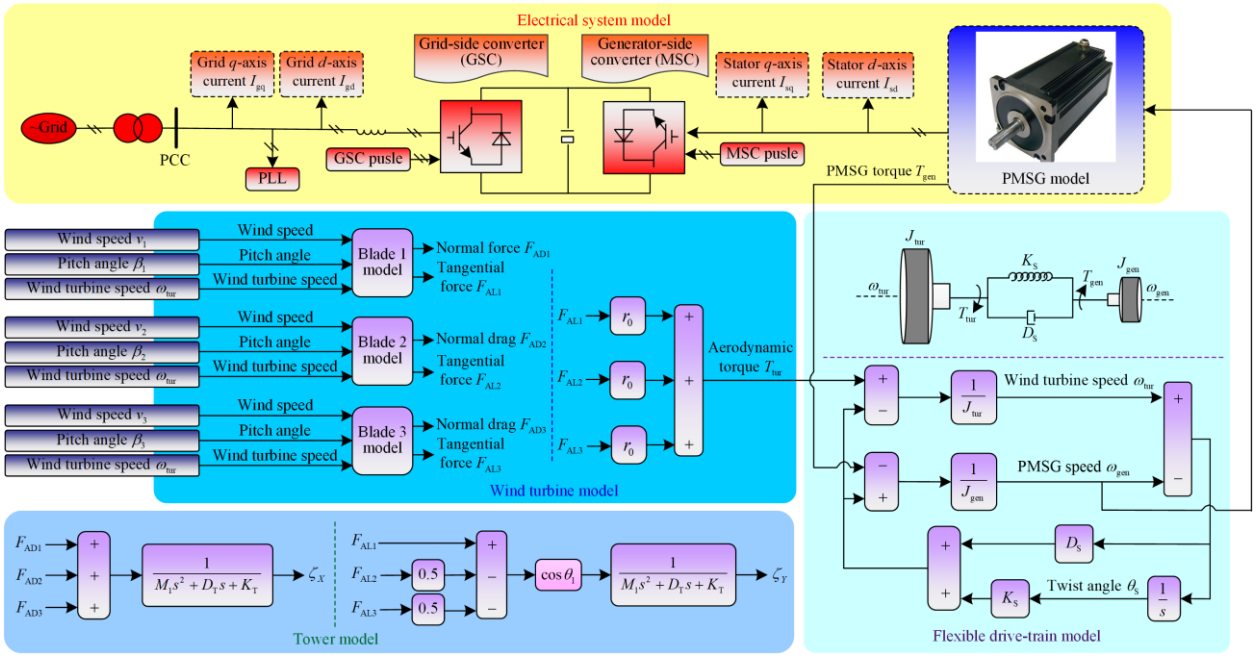

Fig. 4. PMSG-based WECS model.

A. Wind Turbine Model

Based on the analyses of Section II, the aerodynamic normal force $F_{\mathrm{AD}i}$ and tangential force $F_{\mathrm{AL}i}$ on the ith blade can be written as:

$$F_{\mathrm{AD}i} = \int_{r_{\mathrm{hub}}}^{R} 0.5\,W(r)L(r)C_{\mathrm{n}}(r)\mathrm{d}r \tag{9a}$$

$$F_{\mathrm{AL}i} = \int_{r_{\mathrm{hub}}}^{R} 0.5\,W(r)L(r)C_{\mathrm{t}}(r)\mathrm{d}r \tag{9b}$$

where the parameters $W(r)$, $L(r)$, $C_{\mathrm{n}}(r)$, and $C_{\mathrm{t}}(r)$ are the functions of r. According to the integral mean value theorem, r_1 and r_2 can be found by rewriting (9) as:

$$F_{\mathrm{AD}i} = 0.5\,W(r_1)L(r_1)C_{\mathrm{n}}(r_1)(R - r_{\mathrm{hub}}) \tag{10a}$$

$$F_{\mathrm{AL}i} = 0.5\,W(r_2)L(r_2)C_{\mathrm{t}}(r_2)(R - r_{\mathrm{hub}}) \tag{10b}$$

where $r_1 = r_2 = r_0$ is assumed to further simplify the calculation of modeling, and the airfoil curve in r_0 is shown

in Fig. 2(b); F_{ADi} and F_{ALi} will meet $F_{ADi}=kC_n\big|_{\beta=\beta_i}^{v=v_i}$ and $F_{ALi}=kC_t\big|_{\beta=\beta_i}^{v=v_i}$, with $k=0.5WL(R-r_{hub})\big|_{r=r_0}^{v=v_i}$.

B. Flexible Drive-train Model

Given the substantial load carried by the drive-train of a large-scale wind turbine, its flexibility cannot be ignored. Therefore, the double mass spring damping (DMSD) model is generally used to describe the flexible drive-train dynamics [35], given by:

$$J_{tur}\dot{\omega}_{tur}=-D_s(\omega_{tur}-\omega_{gen})-K_s\theta_s+T_{tur} \tag{11a}$$

$$J_{gen}\dot{\omega}_{gen}=D_s(\omega_{tur}-\omega_{gen})+K_s\theta_s-T_{gen} \tag{11b}$$

$$\dot{\theta}_s=\omega_{tur}-\omega_{gen} \tag{11c}$$

where the flexible drive-train parameters are provided in [35]; and the mechanical torque of the wind turbine is expressed as:

$$T_{tur}=\left(F_{AL1}+F_{AL2}+F_{AL3}\right)r_0 \tag{12}$$

C. Tower Model

Due to its large slenderness ratio, low natural frequency, and minimal damping, the flexibility of the tower is also significant and should not be overlooked. As shown in Fig. 5(a), the tower-top motions have two directions: the fore-aft motion along the *X*-axis, and the side-to-side motion along the *Y*-axis. In general, the tower can be represented using the DMSD model, shown in Fig. 5(b).

By the force analysis of mass blocks, the fore-and-aft motion of the tower can be expressed as:

$$M_1\ddot{y}_{X1}+D_T\dot{\zeta}_X+K_T\zeta_X=F_{AD1}+F_{AD2}+F_{AD3} \tag{13a}$$

$$M_2\ddot{y}_{X2}-D_T\dot{\zeta}_X-K_T\zeta_X=-F_X \tag{13b}$$

$$\zeta_X=y_{X1}-y_{X2} \tag{13c}$$

where the mass coefficient of the tower-top mass block M_1 includes the wind turbine nacelle, hub, and blades; and the mass coefficient of the tower-bottom mass block M_2 consists of the tower base and the earth.

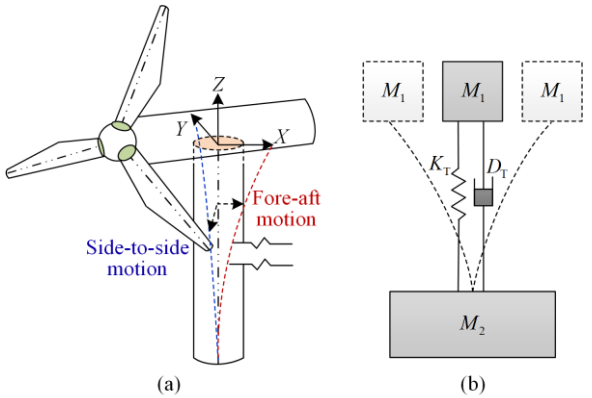

Fig. 5. Tower-top motions and DMSD model. (a) Schematic diagram of tower-top motions. (b) Schematic diagram of DMSD model.

Based on the side-to-side force analysis of the wind wheel shown in Fig. 6, the side-to-side motion of the tower is expressed as:

$$M_1\ddot{y}_{Y1}+D_T\dot{\zeta}_Y+K_T\zeta_Y=\sum_{i=1}^{B}\cos\theta_iF_{ALi}=\cos\theta_1(F_{AL1}-0.5F_{AL2}-0.5F_{AL3}) \tag{14a}$$

$$M_2\ddot{y}_{Y2}-D_T\dot{\zeta}_Y-K_T\zeta_Y=-F_Y \tag{14b}$$

$$\zeta_Y=y_{Y1}-y_{Y2} \tag{14c}$$

In general, due to $M_2\gg M_1$, y_{X2} and y_{Y2} are very small ($y_{X2}\approx 0$ and $y_{Y2}\approx 0$). Thus, by ignoring y_{X2} and y_{Y2}, equations (13) and (14) can be simplified as:

$$M_1\ddot{\zeta}_X+D_T\dot{\zeta}_X+K_T\zeta_X=F_{AD1}+F_{AD2}+F_{AD3} \tag{15a}$$

$$M_1\ddot{\zeta}_Y+D_T\dot{\zeta}_Y+K_T\zeta_Y=\sum_{i=1}^{B}\cos\theta_iF_{ALi}=\cos\theta_1(F_{AL1}-0.5F_{AL2}-0.5F_{AL3}) \tag{15b}$$

From (15b), if $F_{AL1}-0.5F_{AL2}-0.5F_{AL3}\neq 0$, the side-to-side vibration of the tower will be activated.

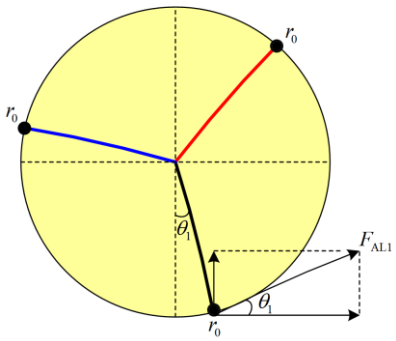

Fig. 6. The side-to-side force analysis of wind wheel.

D. Electrical System Model

The electrical system is generally made up of a PMSG, a back-to-back full power converter, and a power grid. The PMSG model and grid-side power converter dynamics are expressed as [36]:

$$\begin{cases} L_{sd}\dfrac{di_{sd}}{dt}=-R_si_{sd}+L_{sq}n_p\omega_{gen}i_{sq}+u_{sd} \\ L_{sq}\dfrac{di_{sq}}{dt}=-R_si_{sq}-L_{sd}n_p\omega_{gen}i_{sd}-n_p\omega_{gen}\psi+u_{sq} \end{cases} \tag{16a}$$

$$T_{gen}=1.5n_p\left[(L_{sd}-L_{sq})i_{sd}I_{sq}+\psi i_{sq}\right] \tag{16b}$$

$$\begin{cases} L_{gd}\dfrac{di_{gd}}{dt}=-R_gI_{gd}+L_{gq}\omega_gi_{gq}+E_{gd}-u_{gd} \\ L_{gq}\dfrac{di_{gq}}{dt}=-R_gi_{gq}-L_{gd}\omega_gi_{gd}+E_{gq}-u_{gq} \end{cases} \tag{16c}$$

Figure 7 depicts the control blocks of the full power converter in the electrical system. Reference [37] points out that the PMSG dynamic can be considered as a first-order inertia link after the first-order tuning for the PI parameters of the inner loop current control. Since this paper focuses mainly on the tower vibration, the electrical system is appropriately simplified.

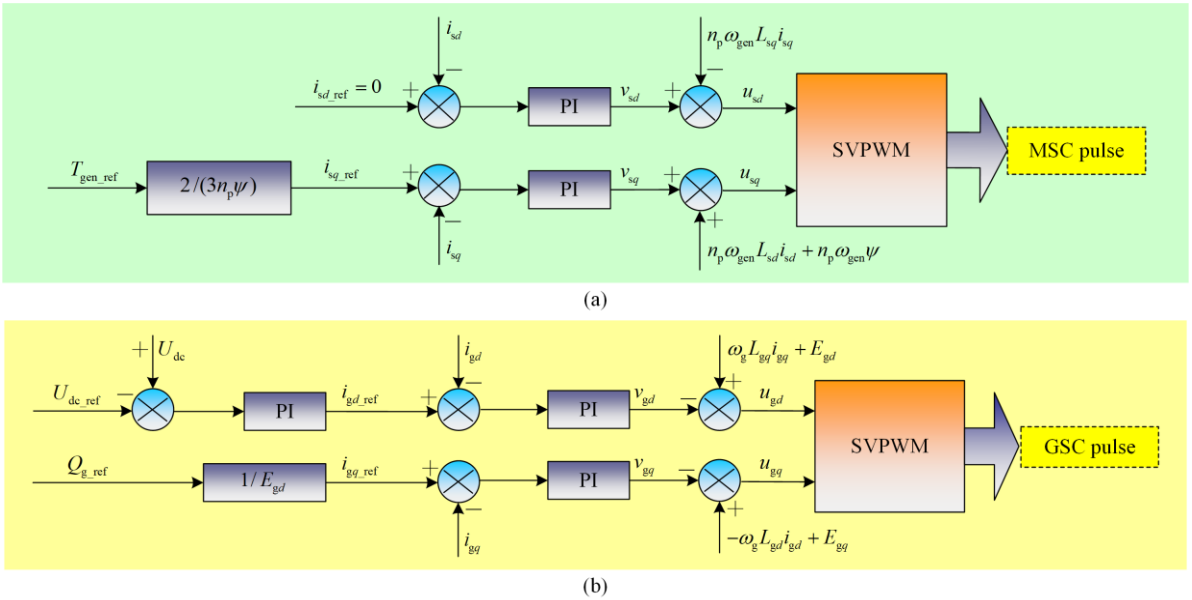

Fig. 7. Full power converter control block.

IV. Torque Control Description and Tower Vibration Analyses

A. Torque Control Description

The Campbell chart shown in Fig. 8 is drawn to analyze the resonance speed of the tower. The 3p frequency component can excite the tower resonance under the maximum power point tracking (MPPT) operation region. This study is mainly concerned with the MPPT control below the rated wind speed. Because the PMSG model and MSC dynamics can be regarded as a first-order inertia link, if the PI parameters are large enough, the dynamic delay of the torque loop can be ignored. Hence, the reference torque T_{ref} is approximately equal to the actual torque T_{gen}. The reference torque under MPPT and the optimal torque coefficient K_{opt} [38]–[40] are expressed as:

$$T_{ref} \approx T_{gen} = K_{opt}\omega_{gen}^2 + T_{Damp} \tag{17a}$$

$$K_{opt} = \rho\pi R^5 C_{P\_max} \big/ \left(2\lambda_{opt}^3\right) \tag{17b}$$

The purpose of introducing T_{Damp} is to control the flexible drive-train torsional vibration, as Fig. 9 illustrates the flexible drive-train damping control.

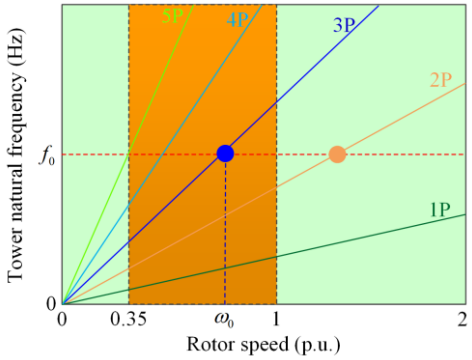

Fig. 8. Campbell chart.

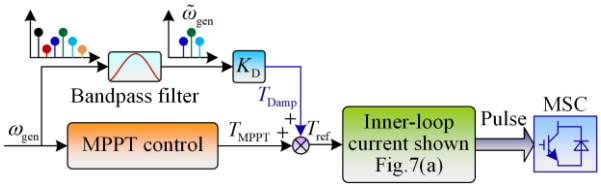

Fig. 9. Flexible drive-train damping control.

Furthermore, due to $J_{tur} \gg J_{gen}$, the wind turbine speed ω_{tur} is very close to the rigid mode. Thus, the drive-train with added damping can be described using the rigid model, as:

$$(J_{tur} + J_{gen})\dot{\omega}_{tur} = T_{tur} - T_{gen} \tag{18}$$

B. Tower Vibration Analyses

From (15) and (A1)–(A10) in the Appendix A, the tower vibration models can be expressed as:

$$M_1\ddot{\tilde{\zeta}}_X + D_T\dot{\tilde{\zeta}}_X + K_T\tilde{\zeta}_X = c_1\sum_{i=1}^{B}\tilde{\beta}_i + Bc_2\tilde{\omega}_{tur} + c_3\sum_{i=1}^{B}\tilde{v}_i \tag{19a}$$

$$M_1\ddot{\tilde{\zeta}}_Y + D_T\dot{\tilde{\zeta}}_Y + K_T\tilde{\zeta}_Y = \cos(\omega_{tur}t+\vartheta)\begin{bmatrix} d_1(\tilde{\beta}_1 - 0.5\tilde{\beta}_2 - 0.5\tilde{\beta}_3) + \\ d_2(\tilde{v}_1 - 0.5\tilde{v}_2 - 0.5\tilde{v}_3) \end{bmatrix} \tag{19b}$$

where c_1, c_2, c_3, d_1, and d_2 are shown in Appendix A; the initial azimuth angle ϑ meets $\theta_1 = \vartheta + \omega_{tur}t$; and the small signal is represented by the superscript '~'. If the collecting variable-pitch mode is adopted ($\beta_i = \beta_c$), equation (19) can be rewritten as:

$$M_1\ddot{\tilde{\zeta}}_X + D_T\dot{\tilde{\zeta}}_X + K_T\tilde{\zeta}_X = Bc_1\tilde{\beta}_c + Bc_2\tilde{\omega}_{tur} + c_3\sum_{i=1}^{B}\tilde{v}_i \tag{20a}$$

$$M_1\ddot{\tilde{\zeta}}_Y + D_T\dot{\tilde{\zeta}}_Y + K_T\tilde{\zeta}_Y = d_2\cos(\omega_{tur}t+\vartheta)(\tilde{v}_1 - 0.5\tilde{v}_2 - 0.5\tilde{v}_3) \tag{20b}$$

From (20a), we know that the changes in β_c, ω_{tur}, and v_i will cause the fore-aft vibration. Equation (20b) indicates the unbalanced wind speed distribution directly induces the side-to-side vibration. When unstable torsional vibration occurs in a flexible drive train, the wind turbine speed ω_{tur} will produce divergent oscillation and the tower vibration will be excited.

C. Influence of WS and TSE on Tower Vibration

It is generally known that the 3p frequency component caused by WS and TSE is the main inducement of wind turbine vibration. Hence, the influence of WS and TSE on tower vibration should be explored. From (12), (17), and (18), the following equation can be obtained:

$$\left[(J_{tur}+J_{gen})s+2K_{opt}\bar{\omega}_{tur}-\frac{Bd_2}{r_0}\right]\tilde{\omega}_{tur}=\frac{1}{r_0}\left(Bd_1\tilde{\beta}_c+d_3\sum_{i=1}^{B}\tilde{v}_i\right) \tag{21}$$

From (21), equation (20a) can be further simplified as:

$$M_1\ddot{\tilde{\zeta}}_X+D_T\dot{\tilde{\zeta}}_X+K_T\tilde{\zeta}_X=\left[Bc_1+G_{F1}(s)\right]\tilde{\beta}_c+\left[c_3+G_{F2}(s)\right]\sum_{i=1}^{B}\tilde{v}_i \tag{22}$$

where $G_{F1}(s)$ and $G_{F2}(s)$, shown in (A11) and (A12) in Appendix A, can be considered as low pass filters. Hence, equation (22) can be simplified as:

$$M_1\ddot{\tilde{\zeta}}_X+D_T\dot{\tilde{\zeta}}_X+K_T\tilde{\zeta}_X=Bc_1\tilde{\beta}_c+c_3\sum_{i=1}^{B}\tilde{v}_i \tag{23}$$

This means that $(\tilde{v}_1-0.5\tilde{v}_2-0.5\tilde{v}_3)\cos\theta_1$ and $\sum_{i=1}^{B}\tilde{v}_i$ are the causes of tower vibration. Generally, the frequencies of turbulent wind are random and time-varying, while the frequencies of shear wind and tower shadow wind contain multiple components corresponding to wind wheel rotation frequency. In addition, the natural damping of the tower is typically very low. With the WECS operating at a certain speed, if the frequencies of shear wind and tower shadow wind coincide with the natural frequency of the tower, resonance in the tower may occur. Therefore, WS and TSE directly contribute to tower vibration. In general, the wind speed on the *i*th blade can be written as:

$$v_i(\theta_i)=v_{hub}+v_{shear}(\theta_i)+v_{tower}(\theta_i) \tag{24}$$

According to [34], $v_{shear}(\theta_i)$ and $v_{tower}(\theta_i)$ can be obtained:

$$v_{shear}(\theta_i)=\frac{2v_{hub}}{R^2-r_{hub}^2}\int_{r_{hub}}^{R}\frac{r^2\mu}{H}\cos\theta_i+\frac{r^3\mu(\mu-1)}{2H^2}\cos^2\theta_i+\frac{r^4\mu(\mu-1)(\mu-2)}{6H^3}\cos^3\theta_i\,\mathrm{d}r \tag{25a}$$

$$v_{tower}(\theta_i)=\frac{2v_{hub}}{R^2-r_{hub}^2}\int_{r_{hub}}^{R}md^2\frac{r^2\sin^2\theta_i-x^2}{(r^2\sin^2\theta_i+x^2)^2}\mathrm{d}r \tag{25b}$$

Because of $\theta_{i+1}=\theta_i+120°$, the azimuth θ_i must meet:

$$\begin{cases}\sum_{i=1}^{3}\cos\theta_i=0\\ \sum_{i=1}^{3}\cos^2\theta_i=\frac{3}{2}\\ \sum_{i=1}^{3}\cos^3\theta_i=\frac{3}{4}\cos3\theta_1\\ \cos\theta_1-0.5\cos\theta_2-0.5\cos\theta_3=2\cos\theta_1\\ \cos^2\theta_1-0.5\cos^2\theta_2-0.5\cos^2\theta_3=\frac{3}{4}\cos2\theta_1\\ \cos^3\theta_1-0.5\cos^3\theta_2-0.5\cos^3\theta_3=\frac{9}{8}\cos\theta_1\end{cases} \tag{26}$$

From (25) and (26), $V_{shear1}=\sum_{i=1}^{B}v_{shear}(\theta_i)$ and $V_{shear2}=\left[v_{shear}(\theta_1)-0.5v_{shear}(\theta_2)-0.5v_{shear}(\theta_3)\right]\cos\theta_1$ can be expressed as (A13) and (A14) in Appendix A. Furthermore, equation (25b) can also be simplified as:

$$v_{tower}(\theta_i)\approx\frac{mv_{hub}}{R^2}\left[\frac{d^2}{\sin^2\theta_i}\ln\left(\frac{R^2\sin^2\theta_i}{x^2}+1\right)-\frac{2d^2R^2}{R^2\sin^2\theta_i+x^2}\right] \tag{27}$$

where $V_{tower1}=\sum_{i=1}^{B}v_{tower}(\theta_i)$; $V_{tower2}=v_{tower}(\theta_1)-0.5v_{tower}(\theta_2)$; while $v_{tower}(\theta_2)-0.5v_{tower}(\theta_3)\cos\theta_1$ can be given by (27).

From (27), (A13), (A14) and the system parameters in Table I, the wind speed variation caused by WS and TSE is shown in Fig.10. As presented in Fig. 10(a), V_{shear1}, V_{tower1}, and their synthetic wind speed contain the 3p frequency component. The phase difference between V_{shear1} and V_{tower1} is π/3. Figure 10(b) indicates that the frequency of V_{tower2} is still the 3p frequency.

TABLE I
SYSTEM PARAMETERS

Symbol	Quantity	Values
μ	Wind shear exponent	0.3
H (m)	Tower height	60
d (m)	Tower radius	2
r_{hub} (m)	Hub radius	2
x (m)	Distance from the blade origin to the tower midline	2.9
M_1 (kg)	Mass coefficient of the tower-top mass block	5×10^4
D_T (N·s·m^{-1})	Tower damping coefficient	9.425×10^3
K_T (N/m)	Tower stiffness coefficient	4.441×10^6
R (m)	Blade length	28
P_{rate} (MW)	Capacity of wind turbine	2

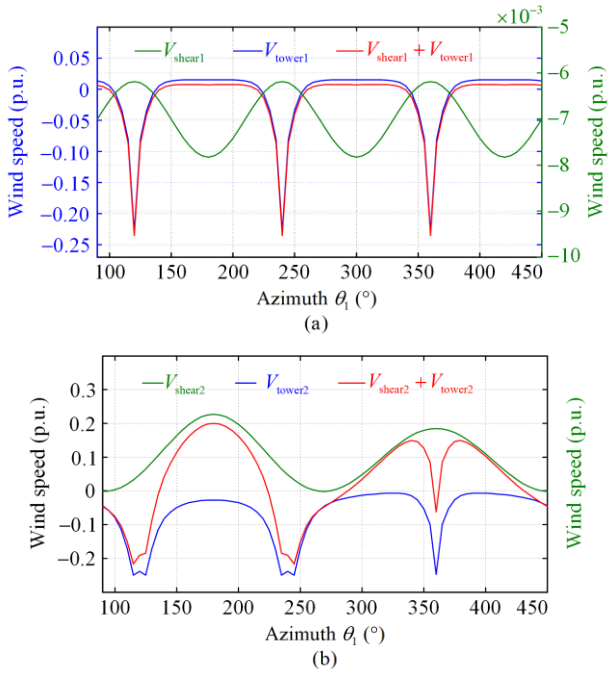

Fig. 10. Wind speed variation because of WS and TSE. (a) Wind speed variation in fore-and-aft direction. (b) Wind speed variation in side-to-side direction.

From (A14) and Fig. 10(b), although the frequencies of V_{shear2} consist of the 1p, 2p, 3p, and 4p frequencies, the 2p frequency is the main form. However, Fig. 8 shows that the 2p frequency component cannot cause tower resonance within the range of rotor speed. Therefore, for both the fore-and-aft tower vibration and the side-to-side tower vibration, it is only necessary to consider the effect of the 3p frequency component.

V. Tower Vibration Suppression

A. Crossing Resonance Zone Method

From the above analyses, the 3p frequency component may cause the tower resonant. It is generally desirable for WECS to quickly cross these resonance points during operation. Figure 11 shows the torque characteristics of WECS. As presented in Fig. 11(a), a unique equilibrium point A_0 exists under the MPPT operation region. The stability of equilibrium point A_0 can be evaluated using the small perturbation method. For instance, if a disturbance results in an increase in speed, the PMSG torque will exceed the wind turbine torque. Consequently, when the disturbance is removed, the WECS will slow down.

Conversely, if a disturbance causes the speed to decrease, the PMSG torque will be less than the wind turbine torque. Thus, the removal of the disturbance would cause the WECS to accelerate. The system will then return to equilibrium A_0, which is a stable operating point.

When the generator torque slope decreases, the working point becomes unstable. Figure 11(b) illustrates that the system will lose stability in case 3. The method of crossing the resonance zone is designed based on this conclusion. As presented in Fig. 11(c), this scheme only needs to modify the PMSG torque curve during $[\omega_P, \omega_S]$. By modifying the optimal torque curve, the system loses stability at working point A_0 and thus quickly passes through the resonance region.

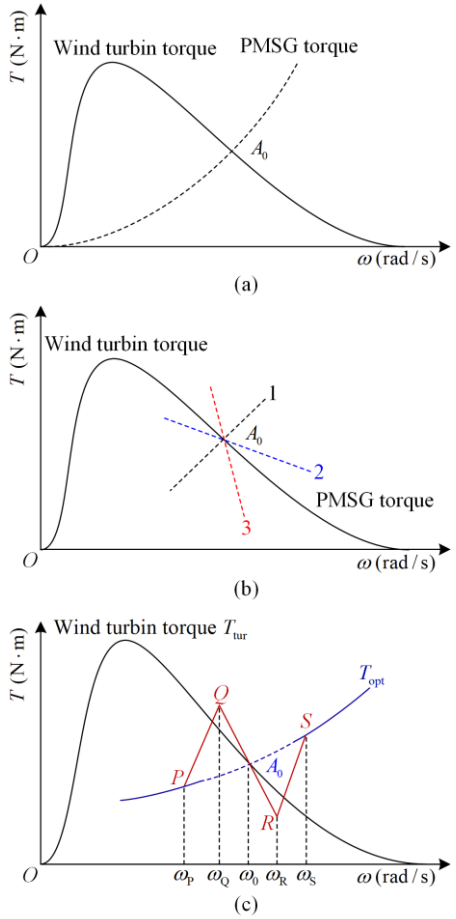

Fig. 11. Torque characteristics curves. (a) Normal torque characteristics under MPPT control. (b) Torque characteristics under different crossing slopes. (c) Corrected torque characteristics.

The slope of wind turbine torque at operating point A_0 is given by:

$$k_A = \left.\frac{\partial T_{tur}}{\partial \omega_{tur}}\right|_{\lambda=\lambda_{opt},\omega=\omega_0} = \left[\frac{\rho\pi R^5 \omega_{tur}}{2\lambda^2}\left(\frac{\partial C_P}{\partial \lambda} - \frac{C_P}{\lambda}\right)\right]\Bigg|_{\lambda=\lambda_{opt},\omega_{tur}=\omega_0} = -\frac{\rho\pi R^5 C_{P\_max}\omega_0}{2\lambda_{opt}^3} \tag{28}$$

The straight line QR slope k_{QR} must meet $k_{QR} < k_A < 0$. In this paper, we set $\omega_P = 2.6$ rad/s, while suggest $\omega_0 = (\omega_P + \omega_R)/2$, $k_{QR} = 40\,k_A$ and

$k_{PQ}=k_{RS}=k_L=-100\,k_A$. At this time, the generator torque T_{gen} meets:

$$T_{ref}\approx T_{gen}=\begin{cases}T_{opt}, & \omega\leqslant\omega_P \text{ or } \omega\geqslant\omega_S\\ k_L(\omega-\omega_P)+K_{opt}\omega_P^2, & \omega_P\leqslant\omega<\omega_Q\\ k_{QR}(\omega-\omega_0)+K_{opt}\omega_0^2, & \omega_Q\leqslant\omega<\omega_R\\ k_L(\omega-\omega_S)+K_{opt}\omega_S^2, & \omega_R\leqslant\omega<\omega_S\end{cases} \quad (29)$$

B. Tower Damping Control

From (23), the collecting pitch control strategy has a direct impact on the fore-aft vibration of the tower. Therefore, the tower damping control can be used in the pitch control loop to suppress the fore-aft vibration of the tower by improving the tower damping. First, equation (23) is rewritten as:

$$\ddot{\tilde{\zeta}}_X+C\dot{\tilde{\zeta}}_X+D\tilde{\zeta}_X=\gamma^-\tilde{\beta}_c+f \quad (30)$$

where C, D, γ^- and f are given as $C=\frac{D_T}{M_1}$, $D=\frac{K_T}{M_1}$, $\gamma^-=\frac{Bc_1}{M_1}<0$, $f=\frac{c_3}{M_1}\sum_{i=1}^{B}\tilde{v}_i$, while f can be considered as an external wind disturbance; and by letting $\tilde{\beta}_c=C_\beta\dot{\tilde{\zeta}}_X$, equation (30) can be further rewritten as:

$$\ddot{\tilde{\zeta}}_X+(C-\gamma^-C_\beta)\dot{\tilde{\zeta}}_X+D\tilde{\zeta}_X=f \quad (31)$$

Damping can be improved by adjusting the parameter C_β. However, this approach has two main disadvantages. First, it is difficult to calculate the parameter γ^- which varies with the operating point and wind speed. Second, this method lacks the necessary robustness against system uncertainties. Therefore, the damper design aims to obtain parameters through extensive tests based on damping performance.

C. Robust Variable-pitch Strategy

In order to overcome the disadvantages of tower damping control, a robust strategy of variable-pitch based on sliding mode control is proposed in this paper to suppress the fore-and-aft tower vibration. By assuming $x=\tilde{\zeta}_X$, $\gamma^+=-\gamma^-$ and $u=-\tilde{\beta}_c$, equation (30) can be rewritten as:

$$\ddot{x}+C\dot{x}+Dx=\gamma^+u+f \quad (32)$$

where γ^+ and f meets $0<\gamma_{min}^+\leqslant\gamma^+\leqslant\gamma_{max}^+$ and $|f|\leqslant F$; γ_{min}^+ and γ_{max}^+ are the minimum and maximum values of γ^+, respectively; while F is the maximum of $|f|$. If the sliding surface S is defined as (33), then the control rate u is expressed as (34).

$$S=\dot{x}+\tau x,\quad \tau>0 \quad (33)$$

$$u=\frac{1}{\gamma_{min}^+}\left[(C-\tau)\dot{x}+Dx-(F+\eta)\operatorname{sgn}(S)\right],\quad \eta>0 \quad (34)$$

where sgn(·) is the symbolic function. If the Lyapunov function is selected as (35), the derivative of V is as (36).

$$V=\frac{1}{2}S^2\geqslant 0 \quad (35)$$

$$\begin{aligned}\dot{V}=S\dot{S}=&\\ &S\left[\gamma^+u+f-(C-\tau)\dot{x}-Dx\right]=\\ &S\left\{\frac{\gamma^+}{\gamma_{min}^+}\left[(C-\tau)\dot{x}+Dx-(F+\eta)\operatorname{sgn}(S)\right]+f-(C-\tau)\dot{x}-Dx\right\}=\\ &S\begin{Bmatrix}\left[\frac{\gamma^+}{\gamma_{min}^+}(C-\tau)-(C-\tau)\right]\dot{x}+\left(\frac{\gamma^+}{\gamma_{min}^+}-1\right)Dx+\\ f-\frac{\gamma^+}{\gamma_{min}^+}(F+\eta)\operatorname{sgn}(S)\end{Bmatrix}=\\ &\left\{\left(\frac{\gamma^+}{\gamma_{min}^+}-1\right)\left[(C-\tau)\dot{x}+Dx\right]S-\frac{\gamma^+}{\gamma_{min}^+}\eta|S|\right\}+\left(fS-\frac{\gamma^+}{\gamma_{min}^+}F|S|\right)\leqslant\\ &\left[\left(\frac{\gamma^+}{\gamma_{min}^+}-1\right)\times|(C-\tau)\dot{x}+Dx|-\frac{\gamma^+}{\gamma_{min}^+}\eta\right]\times|S|+\left(fS-\frac{\gamma^+}{\gamma_{min}^+}F|S|\right)\leqslant\\ &\left[\left(\frac{\gamma_{max}^+}{\gamma_{min}^+}-1\right)\times|(C-\tau)\dot{x}+Dx|-\eta\right]\times|S|+\left(fS-\frac{\gamma^+}{\gamma_{min}^+}F|S|\right)\end{aligned} \quad (36)$$

Because of $fS\leqslant|fS|\leqslant F|S|\leqslant\frac{\gamma^+}{\gamma_{min}^+}F|S|$, if the parameter η meets $\eta\geqslant\left(\frac{\gamma_{max}^+}{\gamma_{min}^+}-1\right)\times|(C-\tau)\dot{x}+Dx|$, the derivative of V meets $\dot{V}\leqslant 0$ and the system meets Lyapunov stability. By assuming (37), the derivative of V meets (38).

$$\eta=\left(\frac{\gamma_{max}^+}{\gamma_{min}^+}-1\right)\times|(C-\tau)\dot{x}+Dx|+\kappa,\quad \kappa>0 \quad (37)$$

$$\dot{V}=\frac{1}{2}\frac{\mathrm{d}}{\mathrm{d}t}S^2\leqslant-\kappa|S| \quad (38)$$

The system trajectory at this time strictly meets the sliding mode condition. Finally, the relay function $\operatorname{relay}(S)=\frac{S}{|S|+a_0}$, $a_0>0$ is used to replace the symbolic function to reduce the chattering of the controller.

VI. Analyses and Validation of Algorithm

Based on the structural model shown in Fig. 3, a simulation test is performed in Matlab/Simulink environment to assess the influence of the 3p frequency component on tower vibration, the method of crossing resonance zone, and the pitch control to suppress the fore-aft tower vibration. Table I shows the system parameters.

A. Influence of 3p Frequency Component on Tower Vibration

According to the tower parameters in Table I, the natural angular frequency of the tower is $\omega_0 = \sqrt{K_T / M_1} \approx 9.42$ rad/s, which means that when the wind turbine speed is close to $\omega_0/3$, the 3p component will excite the tower resonance. The wind speed in the hub center is shown in Fig. 12(a), while the simulation results are presented in Figs. 12 (b)–(d).

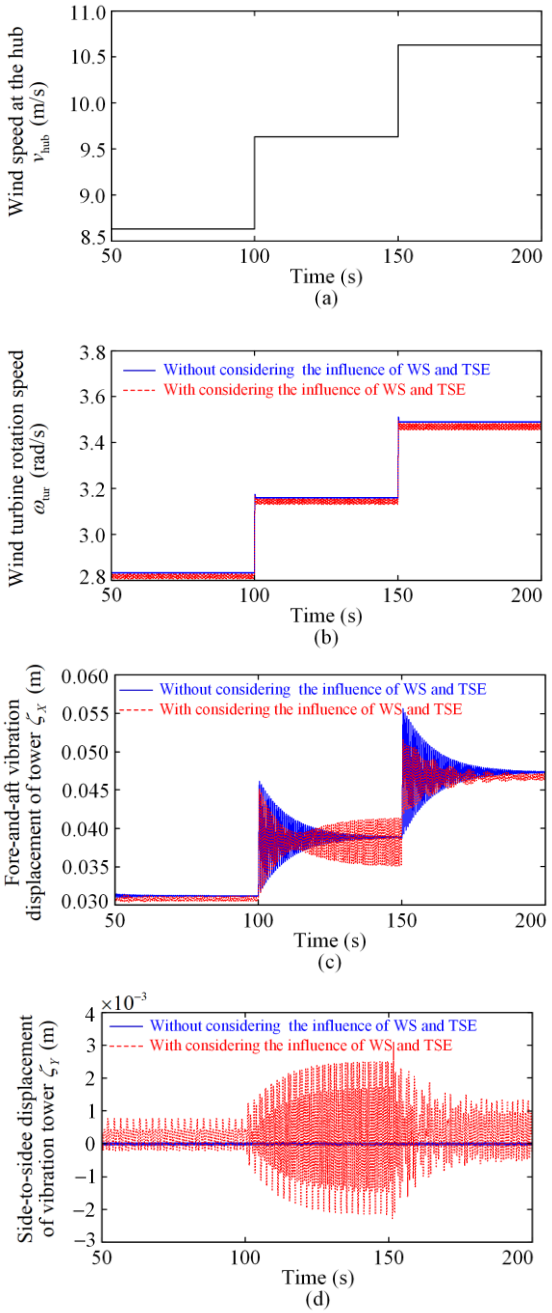

Fig. 12. Influence of WS and TSE on tower vibration. (a) Wind speed curve at the hub. (b) Wind turbine rotation speed curve. (c) Fore-and-aft vibration displacement curve. (d) Side-to-side vibration displacement curve.

The steady-state value of tower vibration amplitude tends towards zero when the influences of WS and TSE are not considered. However, when the effects of WS and TSE are accounted for, the 3p frequency component consistently stimulates tower vibration. When the wind speed in the hub center is close to 9.6 m/s, the tower vibration amplitude is the largest in the steady state, indicating that the 3p frequency component is exciting the tower.

B. Crossing Resonance Zone Method Test

Under the wind conditions shown in Fig. 13(a) and Fig. 14(a), the simulation comparison charts before and after implementing the crossing resonance zone scheme are shown in Figs. 13 (b)–(d) and Figs. 14 (b)–(d).

As depicted in Figs. 13 (b)–(d), without the crossing resonance zone algorithm, the tower resonates when the wind speed is maintained at 9.6 m/s. The crossing resonance zone method ensures that the WECS quickly crosses the resonance zone at this step wind speed, effectively averting tower resonance. In Fig. 14(b), resonance point A is not on the system trajectories when the crossing resonance zone method is adopted. However, as shown in Figs. 14 (c)–(d), the crossing resonance method has negligible effect on the tower vibration under natural wind conditions.

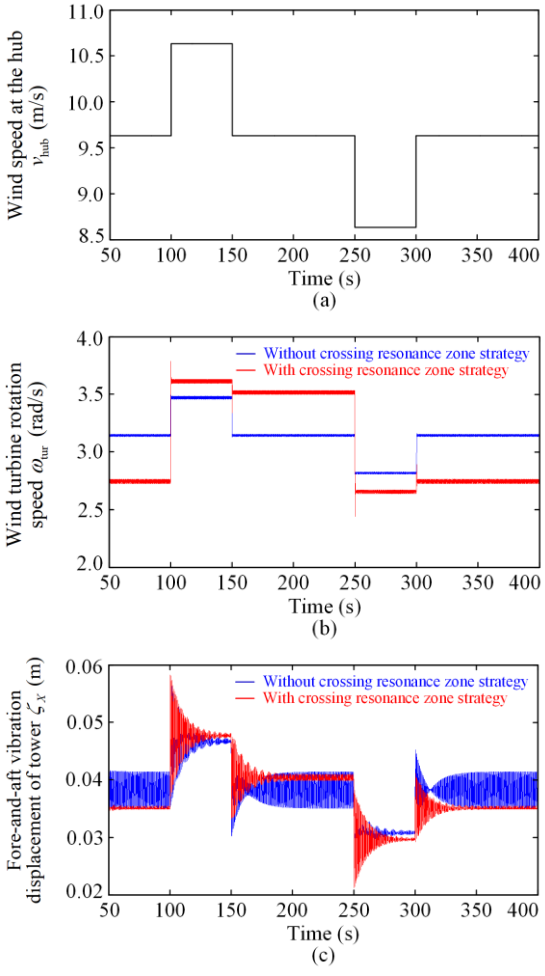

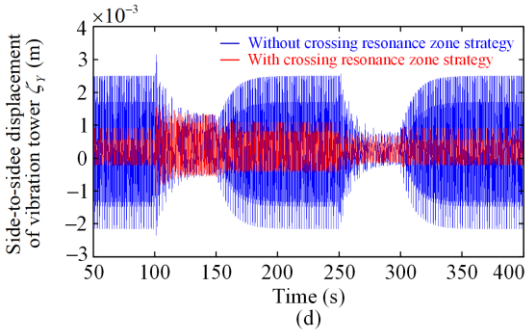

Fig. 13. System response under the step wind speed. (a) Wind speed curve at the hub. (b) Wind turbine rotation speed curve. (c) Fore-and-aft vibration displacement curve. (d) Side-to-side vibration displacement curve.

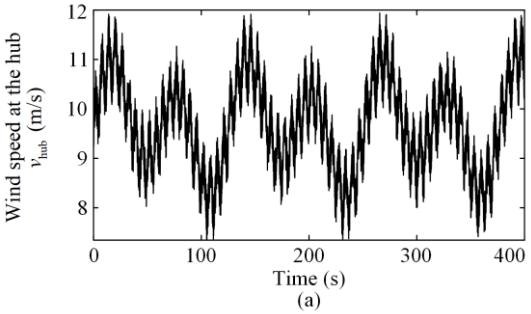

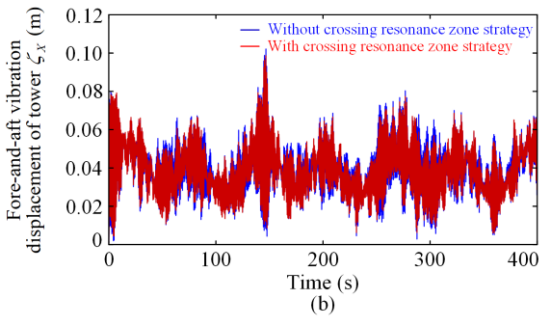

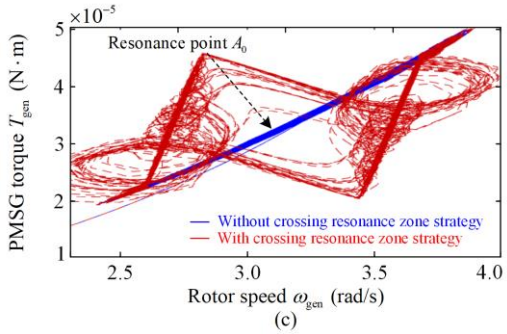

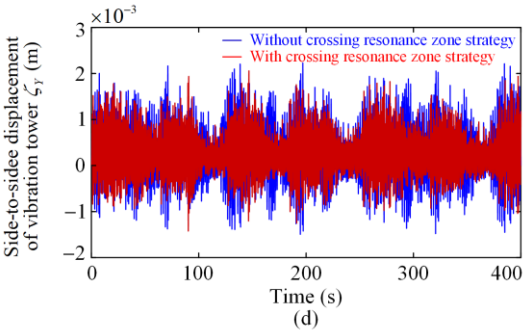

Fig. 14. System response under the natural wind. (a) Wind speed curve at the hub. (b) Fore-and-aft vibration displacement curve. (c) The curve of PMSG torque varying with rotor speed. (d) Side-to-side vibration displacement curve.

C. Pitch Control to Suppress the Tower Vibration Test

The block diagram of controlling the tower vibration is shown in Fig. 15. To verify the effectiveness of the proposed algorithm, a simulation environment is constructed using this basic structure. And the results based on the established simulation model are shown in Figs. 16–18.

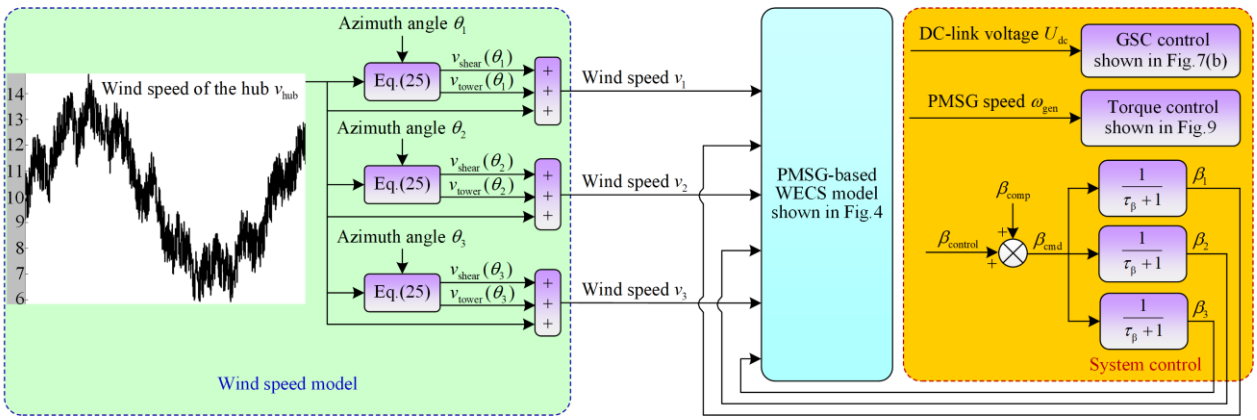

Fig. 15. Block diagram of pitch control to suppress the tower vibration.

Under the step wind condition shown in Fig. 16(a), the wind turbine speed curve, fore-and-aft tower vibration displacement curve, and pitch angle curve are obtained without accounting for the influence of the 3p frequency component on tower vibration, as presented in Figs.16 (b)–(d), respectively. As seen in Fig. 16(c), the proposed robust variable-pitch method based on sliding mode control suppresses the fore-and-aft tower vibration more quickly than the tower damping control.

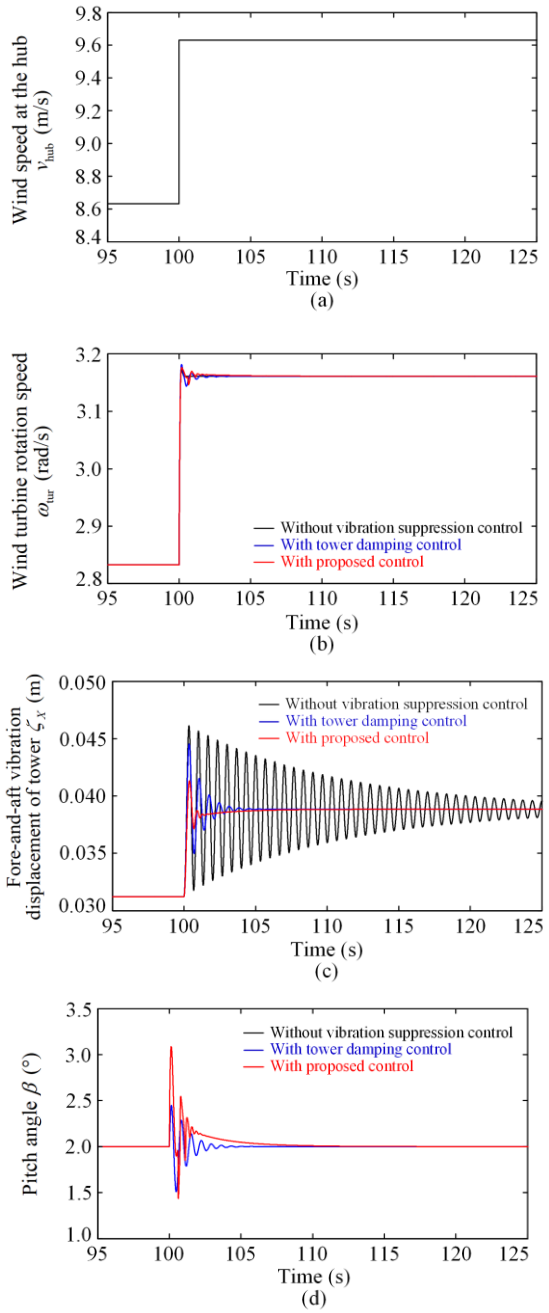

Fig. 16. Tower vibration without considering the influence of the 3p frequency component. (a) Wind speed curve at the hub. (b) Wind turbine rotation speed curve. (c) Fore-and-aft vibration displacement curve. (d) Pitch angle curve.

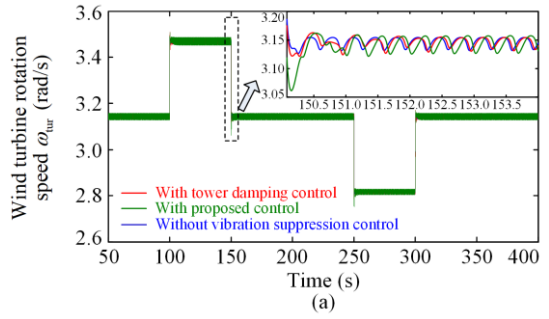

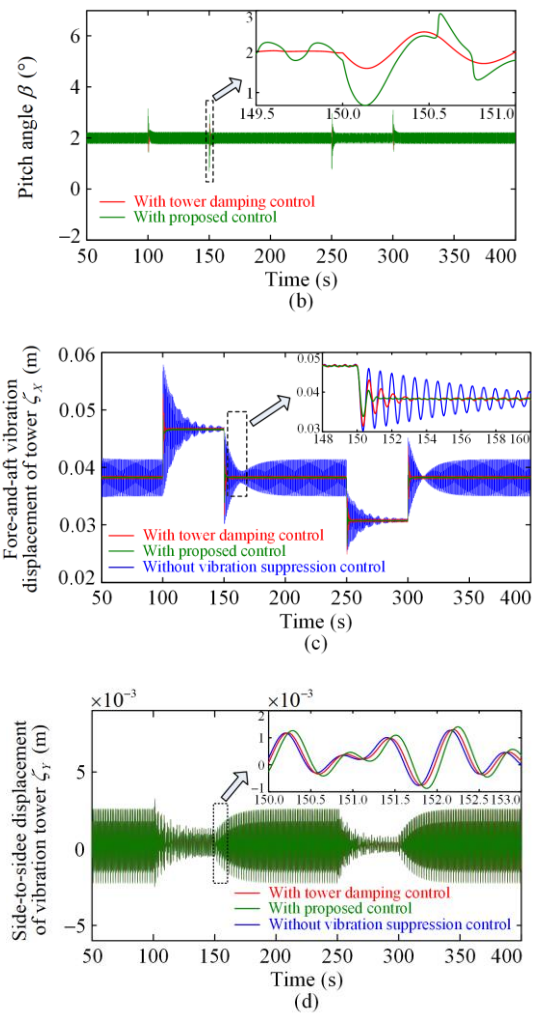

Fig. 17. Tower vibration with considering the influence of 3p frequency component. (a) Wind turbine rotation speed curve. (b) Pitch angle curve. (c) Fore-and-aft vibration displacement curve. (d) Side-to-side vibration displacement curve.

Taking into account the influence of the 3p frequency component on tower vibration and under the wind conditions shown in Fig. 13(a), the wind turbine speed curve, pitch angle curve, fore-and-aft tower vibration displacement curve, and side-to-side tower vibration displacement curve are shown in Figs. 17 (a)–(d), respectively. As depicted in Fig. 17(c), the 3p frequency component does not induce fore-and-aft resonance of the tower under both tower damping control and the proposed control method. Meanwhile, compared with the tower damping control, the proposed robust variable-pitch strategy based on sliding mode control not only suppresses the fore-and-aft tower vibration more quickly but also effectively reduces the influence of the 3p frequency component on such vibration. In Fig. 17(d), both the tower damping control and the proposed robust variable-pitch method based on sliding mode control fail to control the side-to-side tower vibration.

However, since side-to-side tower vibration is only of secondary concern compared to fore-and-aft tower vibration, certain scenarios may only require consideration of the latter.

D. Comparisons of the Fore-and-Aft Tower Vibration Suppression Methods

The suppression effects of fore-and-aft tower vibration are compared here. Figure 18 shows the fore-and-aft tower vibration suppression comparison charts under the natural wind speed conditions presented in Fig. 14(a). The results demonstrate that the proposed robust variable-pitch method based on sliding mode control is the most effective in suppressing fore-and-aft tower vibration.

In Fig. 19, the time window (299 s to 300 s) from Fig. 18 is used to provide a more detailed quantitative analysis of the fore-and-aft tower vibration suppression effect. From Fig. 19, the coordinate data of vibration waveforms can be derived. By examining the coordinate data, it becomes evident that the main frequency of the vibration waveforms is very close to the tower's natural frequency of 1.5 Hz. Next, the waveform change at this natural frequency is analyzed.

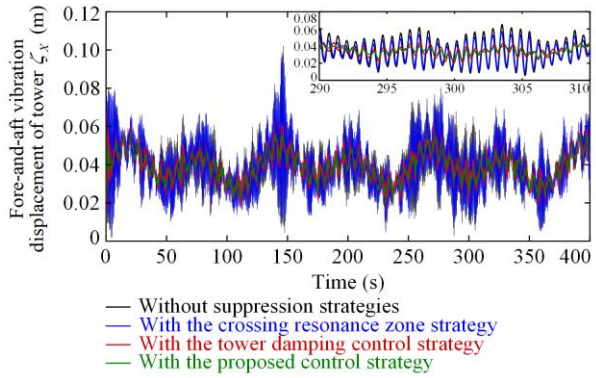

Fig. 18. Comparison charts on the fore-and-aft tower vibration suppression.

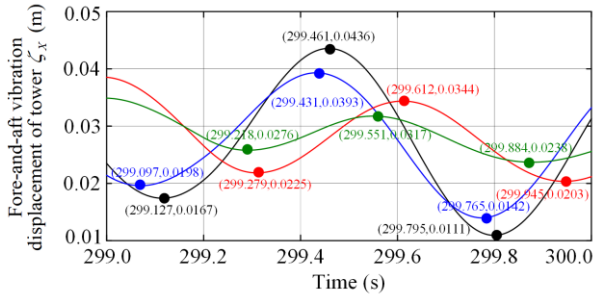

Fig. 19. Time window (299 s to 300 s) in Fig. 18.

As shown in Fig. 20, the blue line represents the vibration waveform while the red line represents slow changes in low-frequency signal. The vibration waveform can be seen as a periodic signal superimposed on the low-frequency signal. We assume that the amplitude of the periodic signal is a_{m}, the coordinates of points A, B_1, and B_2 are known, and the red line can be approximated as a straight line. By the following formula (39), we can derive (40).

$$\begin{cases} Y_{\mathrm{B1}} = -a_{\mathrm{m}} + Y_{\mathrm{C1}} \\ Y_{\mathrm{B2}} = -a_{\mathrm{m}} + Y_{\mathrm{C2}} \\ Y_{\mathrm{A}} = a_{\mathrm{m}} + Y_{\mathrm{D}} \\ Y_{\mathrm{D}} \approx \dfrac{1}{2}(Y_{\mathrm{C1}} + Y_{\mathrm{C2}}) \end{cases} \tag{39}$$

$$a_{\mathrm{m}} \approx \frac{1}{2}Y_{\mathrm{A}} - \frac{1}{4}\left(Y_{\mathrm{B_1}} + Y_{\mathrm{B_2}}\right) \tag{40}$$

where $Y_{\mathrm{A}}, Y_{\mathrm{B1}}, Y_{\mathrm{B2}}, Y_{\mathrm{C1}}, Y_{\mathrm{C2}}$, and Y_{D} are the Y-axis coordinates of points A, B_1, B_2, C_1, C_2, and D, respectively. The vibration amplitude at the natural angular frequency can be obtained using (40). Through calculation, the amplitude of fore-and-aft tower vibration is reduced by about 24.92% under the crossing resonance zone method. Under the tower damping control, the amplitude reducti on reaches 56.23%, while under the proposed robust variable-pitch method, the value is decreased by approximately 79.80%. Meanwhile, from Fig. 21, the percentage amplitude of fore-and-aft tower vibration under natural wind speed can be directly observed. Compared with tower damping control, the suppression ability of the proposed method for fore-and-aft tower vibration is improved by about 53.85% at the natural frequency.

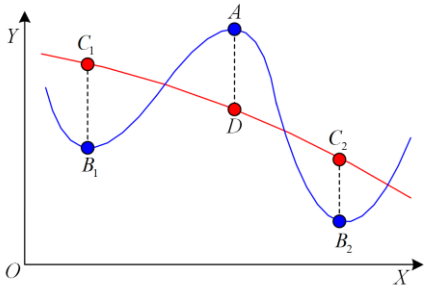

Fig. 20. Coordinate data of the vibration waveform.

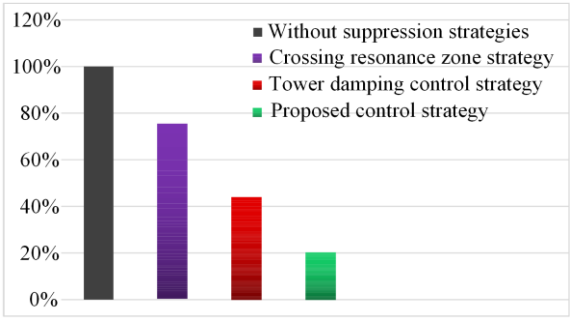

Fig. 21. Percentage amplitude of fore-and-aft tower vibration at the natural frequency.

Finally, power spectral density (PSD) is used to analyze the fore-and-aft tower vibration. Figure 22 presents the PSD values at various frequencies under natural wind speed conditions. For instance, the PSD values in 10 Hz are respectively –80 dB, –80 dB, –93.2 dB, and –99.6 dB. This indicates that under the crossing resonance zone method, the amplitude of fore-and-aft tower vibration is not reduced. Under tower damping control, this amplitude is reduced by about 73.29%, while under the proposed robust variable-pitch method, it is reduced by approximately 85.91%. Compared to tower damping control, the suppression ability of the proposed method for fore-and-aft tower vibration is improved by roughly 47.25 % at the excitation frequency of 10 Hz.

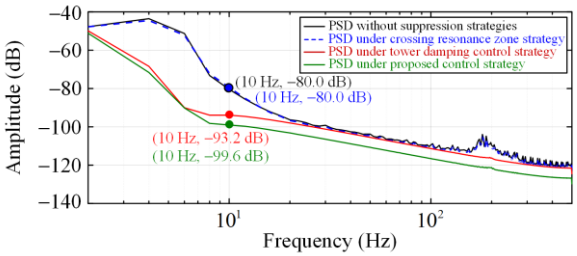

Fig. 22. PSDs under natural wind speed.

VII. Conclusion

With the large-scale development of WECS, tower vibration has become more pronounced, emerging as a significant concern. To analyze the mechanism of tower vibration and develop effective mitigation strategies, this paper has established a mechanism model of tower vibration, comprehensively analyzed the influence of WS and TSE, and proposed a robust approach to suppress tower vibration effectively. Several suppression schemes, including the crossing resonance zone method and the tower damping control, have been evaluated, alongside the proposed variable-pitch method based on sliding mode control. The main conclusions are as follows:

1) The 3p frequency component generated by WS and TSE causes tower resonance when WECS operates at specific speeds. The crossing resonance zone method ensures rapid traversal of the resonance zone, effectively averting tower resonance.

2) The proposed robust variable-pitch method based on sliding mode control not only expedites suppression of fore-and-aft tower vibration but also more effectively reduces the influence of the 3p frequency component on fore-and-aft tower vibration. Compared to tower damping control, the suppression capability of the proposed method for fore-and-aft tower vibration is improved by 53.85% and 47.25% at the natural frequency of 1.5 Hz and excitation frequency of 10 Hz, respectively.

3) Pitch control methods, including tower damping control and the proposed robust variable-pitch scheme, have negligible effect on the suppression of side-to-side tower vibration. There is a need to explore pitch control methods that can effectively suppress fore-and-aft tower vibration and side-to-side tower vibration at the same time.

The future research directions are as follows:

1) Subsequent studies should explore the impact of other uncontrollable factors, such as unpredictable weather conditions, grid voltage dips, and grid voltage imbalance, on tower vibration.

2) The proposed robust control method could be improved to enhance the robustness of the system, mitigating parameter uncertainties and unknown disturbances.

Developing innovative pitch control methods capable of suppressing both fore-and-aft and side-to-side tower vibrations will be a major research focus in future studies.

Appendix A

$$\tilde{F}_{\mathrm{ADi}}=\left.\frac{\partial F_{\mathrm{AD}i}}{\partial \beta_i}\right|_{\beta_i=\bar{\beta}_{\mathrm{c}},v_i=\bar{v}_i,F_{\mathrm{AD}i}=\bar{F}_{\mathrm{AD}}}\tilde{\beta}_i+\left.\frac{\partial F_{\mathrm{AD}i}}{\partial \omega_{\mathrm{tur}}}\right|_{\beta_i=\bar{\beta}_{\mathrm{c}},v_i=\bar{v}_i,F_{\mathrm{AD}i}=\bar{F}_{\mathrm{AD}}}\tilde{\omega}_{\mathrm{tur}}+\left.\frac{\partial F_{\mathrm{AD}i}}{\partial v_i}\right|_{\beta_i=\bar{\beta}_{\mathrm{c}},v_i=\bar{v}_i F_{\mathrm{AD}i}=\bar{F}_{\mathrm{AD}}}\tilde{v}_i \tag{A1}$$

$$\tilde{F}_{\mathrm{AL}i}=\left.\frac{\partial F_{\mathrm{AL}i}}{\partial \beta_i}\right|_{\beta_i=\bar{\beta}_{\mathrm{c}},v_i=\bar{v}_i,F_{\mathrm{AL}i}=\bar{F}_{\mathrm{AL}}}\tilde{\beta}_i+\left.\frac{\partial F_{\mathrm{AL}i}}{\partial \omega_{\mathrm{tur}}}\right|_{\beta_i=\bar{\beta}_{\mathrm{c}},v_i=\bar{v}_i,F_{\mathrm{AL}i}=\bar{F}_{\mathrm{AL}}}\tilde{\omega}_{\mathrm{tur}}+\left.\frac{\partial F_{\mathrm{AL}i}}{\partial v_i}\right|_{\beta_i=\bar{\beta}_{\mathrm{c}},v_i=\bar{v}_i,F_{\mathrm{AL}i}=\bar{F}_{\mathrm{AL}}}\tilde{v}_i \tag{A2}$$

where β_{c} is the pitch angle of collecting variable-pitch; $\bar{F}_{\mathrm{AD}}$ and $\bar{F}_{\mathrm{AL}}$ are given by:

$$\bar{F}_{\mathrm{AD}}=\frac{1}{B}\sum_{i=1}^{B}F_{\mathrm{ADi}}=kC_{\mathrm{n}}\Big|_{\beta=\bar{\beta}_{\mathrm{c}}}^{v=\bar{v}_i} \tag{A3}$$

$$\bar{F}_{\mathrm{AL}}=\frac{1}{B}\sum_{i=1}^{B}F_{\mathrm{AL}i}=kC_{\mathrm{n}}\Big|_{\beta=\bar{\beta}_{\mathrm{c}}}^{v=\bar{v}_i} \tag{A4}$$

In general, due to the inflow angle is small, there are $\sin I\approx I\approx k_1 v_i/\omega_{\mathrm{tur}}$ and $\cos I\approx 1$. In (A5)–(A10), $k=0.5WL(R-r_{\mathrm{hub}})\Big|_{r=r_0}^{v=v_i}$ and $k_1=(1-a)/[(1+b)R]$; $k_{\mathrm{L}j}$ and $k_{\mathrm{D}jj}$ can be found in (5a) and (5b), for example when $a<7.5°$, $j=1$ and $jj=1$, and then $k_{\mathrm{L1}}=0.1267$ and $k_{\mathrm{D1}}=0$.

$$c_1=\left.\frac{\partial F_{\mathrm{AD}i}}{\partial \beta_i}\right|_{\beta_i=\bar{\beta}_{\mathrm{c}},v_i=\bar{v},F_{\mathrm{AD}i}=\bar{F}_{\mathrm{AD}}}=k\frac{\partial C_{\mathrm{n}}}{\partial \beta_i}=k\left(\frac{\partial C_{\mathrm{L}}}{\partial \beta_i}+I\frac{\partial C_{\mathrm{D}}}{\partial \beta_i}\right)=-kk_{\mathrm{L}j}-\frac{kk_{\mathrm{D}jj}k_1\bar{v}}{\bar{\omega}_{\mathrm{tur}}} \tag{A5}$$

$$c_2=\left.\frac{\partial F_{\mathrm{AD}i}}{\partial \omega_{\mathrm{tur}}}\right|_{\beta_i=\bar{\beta}_{\mathrm{c}},v_i=\bar{v},F_{\mathrm{AD}i}=\bar{F}_{\mathrm{AD}}}=C_{\mathrm{n}}\frac{\partial k}{\partial \omega_{\mathrm{tur}}}+k\frac{\partial C_{\mathrm{n}}}{\partial \omega_{\mathrm{tur}}}=\left(C_{\mathrm{L}}+\frac{C_{\mathrm{D}}k_1\bar{v}}{\omega_{\mathrm{tur}}}\right)\frac{k(1+b)\bar{\omega}_{\mathrm{tur}}r_0}{W^2}-\frac{C_{\mathrm{D}}kk_1\bar{v}}{\bar{\omega}_{\mathrm{tur}}^2} \tag{A6}$$

$$c_3=\left.\frac{\partial F_{\mathrm{AD}i}}{\partial v_i}\right|_{\beta_i=\bar{\beta}_{\mathrm{c}},v_i=\bar{v},F_{\mathrm{AD}i}=\bar{F}_{\mathrm{AD}}}=C_{\mathrm{n}}\frac{\partial k}{\partial v_i}+k\frac{\partial C_{\mathrm{n}}}{\partial v_i}=\left(C_{\mathrm{L}}+\frac{C_{\mathrm{D}}k_1\bar{v}}{\bar{\omega}_{\mathrm{tur}}}\right)\frac{k(1-a)\bar{v}}{W^2}+\frac{C_{\mathrm{D}}kk_1}{\bar{\omega}_{\mathrm{tur}}} \tag{A7}$$

$$d_1=\left.\frac{\partial F_{\mathrm{AL}i}}{\partial \beta_i}\right|_{\beta_i=\bar{\beta}_{\mathrm{c}},v_i=\bar{v},F_{\mathrm{AL}i}=\bar{F}_{\mathrm{AL}}}=k\frac{\partial C_{\mathrm{t}}}{\partial \beta_i}=k\left(I\frac{\partial C_{\mathrm{L}}}{\partial \beta_i}-\frac{\partial C_{\mathrm{D}}}{\partial \beta_i}\right)=-\frac{kk_{\mathrm{L}j}k_1\bar{v}}{\bar{\omega}_{\mathrm{tur}}}-kk_{\mathrm{D}jj} \tag{A8}$$

$$d_2=\left.\frac{\partial F_{\mathrm{AL}i}}{\partial \omega_{\mathrm{tur}}}\right|_{\beta_i=\bar{\beta}_{\mathrm{c}},v_i=\bar{v}_i,F_{\mathrm{AL}i}=\bar{F}_{\mathrm{AL}}}=C_{\mathrm{t}}\frac{\partial k}{\partial \omega_{\mathrm{tur}}}+k\frac{\partial C_{\mathrm{t}}}{\partial \omega_{\mathrm{tur}}}=\left(\frac{C_{\mathrm{L}}k_1\bar{v}}{\bar{\omega}_{\mathrm{tur}}}-C_{\mathrm{D}}\right)\frac{k(1+b)\bar{\omega}_{\mathrm{tur}}r_0}{W^2}-\frac{C_{\mathrm{L}}kk_1\bar{v}}{\bar{\omega}_{\mathrm{tur}}^2} \tag{A9}$$

$$d_3=\left.\frac{\partial F_{\mathrm{AL}i}}{\partial v_i}\right|_{\beta_i=\bar{\beta}_{\mathrm{c}},v_i=\bar{v},F_{\mathrm{AL}i}=\bar{F}_{\mathrm{AL}}}=C_{\mathrm{t}}\frac{\partial k}{\partial v_i}+k\frac{\partial C_{\mathrm{t}}}{\partial v_i}=\left(\frac{C_{\mathrm{L}}k_1\bar{v}}{\bar{\omega}_{\mathrm{tur}}}-C_{\mathrm{D}}\right)\frac{k(1+a)\bar{v}}{W^2}+\frac{C_{\mathrm{L}}kk_1}{\bar{\omega}_{\mathrm{tur}}} \tag{A10}$$

$$G_{\mathrm{F1}}(s)=\frac{B^2d_1c_2}{(J_{\mathrm{tur}}+J_{\mathrm{gen}})r_0s+2r_0K_{\mathrm{opt}}\bar{\omega}_{\mathrm{tur}}-Bd_2} \tag{A11}$$

$$G_{\mathrm{F2}}(s)=\frac{Bc_2d_3}{(J_{\mathrm{tur}}+J_{\mathrm{gen}})r_0s+2r_0K_{\mathrm{opt}}\bar{\omega}_{\mathrm{tur}}-Bd_2} \tag{A12}$$

$$V_{\mathrm{shear1}}=\sum_{i=1}^{B}v_{\mathrm{shear}}(\theta_i)=\frac{3v_{\mathrm{hub}}}{R^2-r_{\mathrm{hub}}^2}\times\left[\begin{array}{l}\frac{(R^4-r_{\mathrm{hub}}^4)\mu(\mu-1)}{8H^2}+\\ \frac{(R^5-r_{\mathrm{hub}}^5)\mu(\mu-1)(\mu-2)}{60H^3}\cos\theta_1\end{array}\right]\approx 3v_{\mathrm{hub}}\left[\begin{array}{l}\frac{\mu(\mu-1)}{8}\left(\frac{R}{H}\right)^2+\\ \frac{\mu(\mu-1)(\mu-2)}{60}\left(\frac{R}{H}\right)^3\cos 3\theta_1\end{array}\right] \tag{A13}$$

$$V_{\mathrm{shear2}}=\left[v_{\mathrm{shear}}(\theta_1)-0.5v_{\mathrm{shear}}(\theta_2)-0.5v_{\mathrm{shear}}(\theta_3)\right]\cos\theta_1=\frac{2v_{\mathrm{hub}}}{R^2-r_{\mathrm{hub}}^2}\left[\begin{array}{l}\frac{3(R^4-r_{\mathrm{hub}}^4)\mu(\mu-1)}{64H^2}\cos 3\theta_1+\\ \left(\begin{array}{l}\frac{(R^3-r_{\mathrm{hub}}^3)\mu}{3H}+\frac{3}{160H^3}\times\\ (R^5-r_{\mathrm{hub}}^5)\mu(\mu-1)(\mu-2)\end{array}\right)\cos 2\theta_1+\\ \frac{3(R^4-r_{\mathrm{hub}}^4)\mu(\mu-1)}{64H^2}\cos\theta_1+\\ \frac{3(R^5-r_{\mathrm{hub}}^5)\mu(\mu-1)(\mu-2)}{160H^3}+\frac{(R^3-r_{\mathrm{hub}}^3)\mu}{3H}\end{array}\right]\approx 2v_{\mathrm{hub}}\left[\begin{array}{l}\frac{3R^2\mu(\mu-1)}{64H^2}\cos 3\theta_1+\left(\frac{R\mu}{3H}+\frac{3R^3\mu(\mu-1)(\mu-2)}{160H^3}\right)\\ \cos 2\theta_1+\frac{3R^2\mu(\mu-1)}{64H^2}\cos\theta_1+\\ \frac{3R^3\mu(\mu-1)(\mu-2)}{160H^3}+\frac{R\mu}{3H}\end{array}\right] \tag{A14}$$

ACKNOWLEDGMENT

Not applicable.

AUTHORS' CONTRIBUTIONS

Feihang Zhou: conceptualization, methodology, and validation. Ji Pang: writing original draft preparation. Bo Wang: writing-reviewing, editing, and supervision. Jianxiang Yang: editing and supervision. All authors read and approved the final manuscript.

FUNDING

This work is supported by the Natural Science Foundation of Shaanxi Province (No. 2023-JC-QN-0515 and No. 2023-JC-QN-0534) and Guangdong Basic and Applied Basic Research Foundation (No. 2024A1515011580), and partially supported by Shaanxi Provincial Department of Education Project (No. 23JK0660) and the Xi'an Municipal Bureau of Science and Technology (No. 24GXF0085).

AVAILABILITY OF DATA AND MATERIALS

Not applicable.

DECLARATIONS

Competing interests: The authors declare that they have no known competing financial interests or personal relationships that could have appeared to influence the work reported in this article.

AUTHORS' INFORMATION

Feihang Zhou was born in October 1989, graduated from Xi'an University of Technology in China and received the Ph.D. degree. He is a lecturer of Xi'an

University of Posts & Telecommunications now and is actively involved in postdoctoral research at the Postdoctoral Research Station of Electrical Engineering, Xi'an University of Technology. His research focuses on the suppression of power system oscillation and wind turbine.

Ji Pang received the B.S., M.S., and Ph.D. degrees in electrical engineering from Northwestern Polytechnical University, Xi'an, China, in 2012, 2015, 2020 respectively. He is an associate professor in Department of Automation School at Xi'an University of Posts & Telecommunications, Xi'an, China.

Bo Wang was born in 1986, Xi'an, China. He received the B.S. degree from Xi'an University of Technology of Xi'an, Shaanxi, China, in 2008. He received the M.S degree and Ph.D. degree from Xidian University, Xi'an, Shaanxi, China, in 2011 and 2016, respectively. He is currently a lecture of Xi'an University of Posts and Telecommunications. His research interest is RFID reader, tag antenna design and measurement. His currently research interest includes wireless and chipless tag sensor.

Jianxiang Yang received the mechanical engineering Master's degree from Guilin University of Electronic Technology, Guilin, China, in 2013, and received the Ph.D. degree in mechanical and electronic engineering from Xi'an University of Technology. He is a lecturer in the School of Automation at Guangdong Polytechnic Normal University, Guangzhou,, China. His research interest includes wind turbine vibration analysis and adaptive control of complex dynamical systems.

REFERENCES

[1] D. Song, S. Xu, and L. Huang *et al.*, "Multi-site and multi-objective optimization for wind turbines based on the design of virtual representative wind farm," *Energy*, vol. 252, Aug. 2022.

[2] M. H. El-Bahay, M. E. Lotfy, and M. A. El-Hameed *et al.*, "Effective participation of wind turbines in frequency control of a two-area power system using coot optimization," *Protection and Control of Modern Power Systems*, vol. 8, no. 1, pp. 1-15, Jan. 2023.

[3] F. Zhou, J. Yang, and J. Pang *et al.*, "Research on control methods and technology for reduction of large-scale wind turbine blade vibration," *Energy Reports*, vol. 9, pp. 912-923, Dec. 2023.

[4] D. Song, Y. Tu, and L. Wang *et al.*, "Coordinated optimization on energy capture and torque fluctuation of wind turbines via variable weight NMPC with fuzzy regulator," *Applied Energy*, vol. 312, Apr. 2022.

[5] P. Dao, "On Wilcoxon rank sum test for condition monitoring and fault detection of wind turbines," *Applied Energy*, vol. 318, Jul. 2022.

[6] F. Zhou, "Drive-train torsional vibration suppression of large scale PMSG-based WECS," *Protection and Control of Modern Power Systems*, vol. 7, no. 3, pp. 1-13, Jul. 2022.

[7] Z. Tang, J. Liu, and J. Ni *et al.*, "Power prediction of wind farm considering the wake effect and its boundary layer compensation," *Protection and Control of Modern Power Systems*, vol. 9, no. 6, pp. 19-29, Nov. 2024.

[8] C. J. Spruce and J. K. Turner, "Tower vibration control of active stall wind turbines," *IEEE Transactions on Control Systems Technology*, vol. 21, no. 4, pp. 1049-1066, Jul. 2013.

[9] W. H. Lio, B. L. Jones, and J. A. Rossiter, "Estimation and control of wind turbine tower vibrations based on individual blade-pitch strategies," *IEEE Transactions on Control Systems Technology*, vol. 27, no. 4, pp. 1820-1828, Jul. 2019.

[10] Z. Han, Z. Liu, and K. Wen *et al.*, "Boundary feedback control of a nonhomogeneous wind turbine tower with exogenous disturbances," *IEEE Transactions on Automatic Control*, vol. 67, no. 4, pp. 1952-1959, Apr. 2022.

[11] L. Ren, H. Yang, and S. Liu *et al.*, "Passivity based control of tower vibration of onshore wind turbines," in *34th Chinese Control Conference (CCC)*, Hangzhou, China, Sep. 2015, pp. 934-939.

[12] H. Tian, M. N. Soltani, and M. E. Nielsen, "Review of floating wind turbine damping technology," *Ocean Engineering*, vol. 278, Jun. 2023.

[13] P. Martynowicz, "Nonlinear optimal-based vibration control of a wind turbine tower using hybrid vs. magnetorheological tuned vibration absorber," *Energies*, vol. 14, no. 16, Aug. 2021.

[14] F. Golnary and K. T. Tse, "Simultaneous active control of tower lateral vibration and power control of wind turbine: a novel multivariable approach," *Energy Reports*, vol. 8, pp. 4233-4251, Nov. 2022.

[15] W. He and S. Ge, "Vibration control of a nonuniform wind turbine tower via disturbance observer," *IEEE/ASME Transactions on Mechatronics*, vol. 20, no. 1, pp. 237-244, Feb. 2015.

[16] M. I. G. Planas and B. M. Valiente, "Stability analysis of a wind turbine tower using reachability properties of switched systems," *IEEE Latin America Transactions*, vol. 13, no.7, pp. 2252-2257, Jul. 2015.

[17] A. Hu, J. Zhao, and L. Xiang, "Output-only modal analysis of wind turbine tower based on vibration response under emergency stop," *ISA Transactions*, vol. 80, pp. 411-426, Sep. 2018.

[18] J. Feliciano, G. Cortina, and A. Spear *et al.*, "Generalized analytical displacement model for wind turbine towers under aerodynamic loading," *Journal of Wind Engineering & Industrial Aerodynamics*, vol. 176, pp. 120-130, May 2018.

[19] S. Sarkar and B. Fitzgerald, "Fluid inerter for optimal vibration control of floating offshore wind turbine towers," *Engineering Structures*, vol. 266, Sep. 2022.

[20] B. Zhang, Y. Jin, and S, Cheng *et al*., "On the dynamics of a model wind turbine under passive tower oscillations," *Applied Energy*, vol. 311, Apr. 2022.

[21] H. Zuo, K. Bi, and H. Hao *et al*., "Numerical study of using shape memory alloy-based tuned mass dampers to control seismic responses of wind turbine tower," *Engineering Structures*, vol. 250, Jan. 2022.

[22] M. Lara, J. Garrido, and M. L. Ruz *et al*., "Multi-objective optimization for simultaneously designing active control of tower vibrations and power control in wind turbines," *Energy Reports*, vol. 9, pp. 1637-1650, Dec. 2023

[23] P. J. Murtagh, A. Ghosh, and B. Basu *et al.*, "Passive control of wind turbine vibrations including blade/tower interaction and rotationally sampled turbulence," *Wind Energy*, vol. 11, no. 4, pp. 305-317, Oct. 2008.

[24] B. Fitzgerald, S. Sarkar, and A. Staino, "Improved reliability of wind turbine towers with active tuned mass dampers (ATMDs)," *Journal of Sound & Vibration*, vol. 419, pp. 103-122, Apr. 2018.

[25] E. Mohammadi, R. Fadaeinedjad, and G. Moschopoulos, "Implementation of internal model based control and individual pitch control to reduce fatigue loads and tower vibrations in wind turbines," *Journal of Sound & Vibration*, vol. 421, pp. 132-152, May 2018.

[26] A. Bajric, J. Hogsberg, and F. Rüdinger, "Evaluation of damping estimates by automated operational modal analysis for offshore wind turbine tower vibrations," *Renewable Energy*, vol. 116, pp. 153-163, Feb. 2018.

[27] J. G. Simpson, M. Kaminski, and E. Loth, "Influence of tower shadow on downwind flexible rotors: Field tests and simulations," *Wind Energy*, vol. 25, no. 5, pp. 881-896, May 2022.

[28] Y. Liu, Y. Qiao, and S. Han *et al.*, "Rotor equivalent wind speed calculation method based on equivalent power considering wind shear and tower shadow," *Renewable Energy*, vol. 172, pp. 882-896, Jul. 2021.

[29] R. Fadaeinedjad, G. Moschopoulos, and M. Moallem, "The impact of tower shadow, yaw error, and wind shears on power quality in a wind–diesel system," *IEEE Transactions on Energy Conversion*, vol. 24, no. 1, pp. 102-111, Jan. 2009.

[30] J. Liu, F. Zhou, and F. Liu, "Analysis and restraining of permanent magnet synchronous wind turbine shaft vibration," *Transactions of China Electrotechnical Society*, vol. 33, no. 4, pp. 930-942, Feb. 2018.

[31] M. Chetan, M. S. Sakib, and D. T. Griffith *et al.*, "Design of a 3.4-MW wind turbine with integrated plasma actuator-based load control," *Wind Energy*, vol. 25, no. 3, pp. 517-536, Mar. 2022.

[32] T. Thiringer and J. A. Dahlberg, "Periodic pulsations from a three-bladed wind turbine," *IEEE Transactions on Energy Conversion*, vol. 16, no. 2, pp. 128-133, Jun. 2001.

[33] P. Sorensen, A. D. Hansen, and P. A. C. Rosas, "Wind models for simulation of power fluctuations from wind farms," *Journal of Wind Engineering & Industrial Aerodynamics*, vol. 90, pp. 1381-1402, Dec. 2002.

[34] D. S. L. Dolan, and P. W. Lehn, "Simulation model of wind turbine 3p torque oscillations due to wind shear and tower shadow," *IEEE Transactions on Energy Conversion*, vol. 21, no. 3, pp. 717-724, Sep. 2006.

[35] J. Liu, F. Zhou, and C. Zhao *et al*, "Mechanism analysis and suppression strategy research on permanent magnet synchronous generator wind turbine torsional vibration," *ISA Transactions*, vol. 92, pp. 118-133, Sep. 2019.

[36] B. Ren, Q. Li, and Q. Zhou *et al*., "Analysis and comparison of multi-parameter factors affecting the stability of subsynchronous oscillation of grid-connected PMSG," *Energy Reports*, vol. 8, pp. 51-58. Aug. 2022.

[37] F. Zhou and J. Liu, "Pitch controller design of wind turbine based on nonlinear PI/PD control," *Shock and Vibration*, vol. 10, pp. 1-14, Oct. 2018.

[38] Z. R. Labidi, H. Schulte and A. Mami, "Modeling and optimal torque control of small wind turbines with permanent magnet synchronous generators," in *2017 International Conference on Green Energy Conversion Systems (GECS)*, Hammamet, Tunisia, Mar. 2017, pp. 1-6.

[39] X. Deng, J. Yang, and Y. Sun *et al.*, "An effective wind speed estimation based extended optimal torque control for maximum wind energy capture," *IEEE Access*, vol. 8, pp. 65959-65969, Apr. 2020.

[40] K. H. Kim, T. L. Van, and D. C. Lee *et al.*, "Maximum output power tracking control in variable-speed wind turbine systems considering rotor inertial power," *IEEE Transactions on Industrial Electronics*, vol. 60, no. 8, pp. 3207-3217, Aug. 2013.